Limit on the electric-dipole moment of ^{199}Hg using synchronous optical pumping

J. P. Jacobs,* W. M. Klipstein, S. K. Lamoreaux, B. R. Heckel, and E. N. Fortson
Department of Physics, FM-15, University of Washington, Seattle, Washington 98195
(Received 1 June 1995)

Synchronously driven optically pumped atomic oscillators have been used to measure the electric-dipole moment of ^{199}Hg as a test of time-reversal symmetry. Our result, $d(^{199}\mathrm{Hg}) < 8.7\times 10^{-28} e$ cm, is the smallest experimental limit on the size of an electric-dipole moment and sets stringent bounds on several sources of time-reversal symmetry violation in atomic systems. This article describes the details of the experimental apparatus, the measurement procedure, and the implications of the result for CP violation in elementary particle interactions.

PACS number(s): 11.30.Er, 32.10.Dk, 32.80.Bx

No permanent electric-dipole moment (EDM) of an elementary particle, atom, or molecule has yet been detected after several decades of experimentation. The existence of such a dipole would imply a breakdown of time-reversal symmetry T and, through the CPT theorem, a breakdown in CP, the combined symmetries of charge conjugation and parity. The only known example of CP violation in nature, discovered 30 years ago [1], occurs in the decay of the K_0 meson. Historically, most theories put forth to account for the K_0 experiments have been ruled out by upper limits set on the EDM of the neutron [2]. Atomic and molecular EDM experiments, based on a variety of techniques [3–6], have become another important probe of CP violation. Recent EDM limits on mercury [7], thallium fluoride [8], cesium [9], and thallium [10], as well as the neutron [11,12], test CP symmetry on a broad front and set stringent bounds on CP violation in leptonic, semileptonic, and hadronic interactions.

It is now generally accepted that a satisfactory explanation of CP violation in the K_0 system is given by the standard model [13], in which CP violation occurs as a phase factor in the interaction of quarks with W bosons. Because this model by itself predicts EDM's too small to be observed in current or contemplated experiments, EDM experiments are now considered an ideal probe for evidence of new physics and new sources of CP violation. If an EDM is found, it will be compelling evidence for the existence of some sort of new physics beyond the standard model. Conversely, to the extent that an EDM is not seen in increasingly sensitive experiments, some proposed models of new physics such as low-energy supersymmetry or multi-Higgs theories may have to be given up [13,33].

In a recent publication [7], we reported the results of an experiment to search for an EDM of the ^{199}Hg atom, which improved on our earlier mercury experiment [14] (hereafter called HG1) by a factor of 25, and set important new bounds on CP-violating quark-quark and electron-quark interactions. In this paper we describe this experiment (HG2) in some detail and include the latest data to obtain the current best limit on the mercury EDM. We also consider the implications of this limit for models of CP violation. The paper is divided into seven sections: I is the introduction; II discusses transverse synchronous optical pumping; III describes the experimental apparatus; IV refers to data acquisition and analysis; V discusses systematic effects; VI gives the results; and VII details the theoretical implications. There are three Appendixes: A describes the system noise; B describes the Hg vapor cells; and C contains a calculation of the effect of a magnetic field gradient.

I. INTRODUCTION

Atomic and molecular EDM experiments fall naturally into two classes, those sensitive to the electron spin and those sensitive to the nuclear spin. The former test leptonic sources of T violation, the latter test hadronic sources, while both are sensitive to T violation in lepton-hadron coupling.

^{199}Hg is close to an ideal choice of atom for a nuclear-spin experiment. Mercury is a heavy atom, and as shown by Sandars [4], the effect of T violation can be greatly enhanced in heavy atoms. All presently considered sources of T violation produce an atomic EDM that grows rapidly with the nuclear charge, scaling roughly as Z^2 for nuclear-spin-dependent effects. In addition, ^{199}Hg has no electronic angular momentum in its $6\,^1S_0$ ground state, and the spin-$\frac{1}{2}$ nucleus has no electric quadrupole interaction; this permits long nuclear-spin relaxation lifetimes inside ^{199}Hg vapor cells and correspondingly high sensitivity to any small spin precession induced by an EDM in an external electric field. Furthermore, the population of nuclear-spin states can be efficiently polarized in a reasonably dense ($>10^{13}$ atoms/cm^3) ^{199}Hg vapor by using ground state optical pumping on the 254-nm intercombination line, and the spin direction can be monitored optically on the same line, leading to experimental simplicity and high inherent statistical accuracy.

As a vector operator, an EDM must point along the total angular momentum. The Hamiltonian for a ^{199}Hg atom in external electric and magnetic fields, $\mathbf{E}$ and $\mathbf{B}$, is then

$$H = -(d\mathbf{E} + \mu\mathbf{B})\cdot\mathbf{I}/I, \tag{1}$$

where d and μ are the electric and magnetic-dipole moments, and $I = 1/2$ is the nuclear spin. The violation of T in

*Present address: Department of Physics and Astronomy, University of Montana, Missoula, Montana 59812.

Eq. (1) is evident, since **E** does not change sign under $t \rightarrow -t$, whereas **B** and **I** both do; only if $d=0$ will H be invariant under time reversal.

We measure the EDM by observing the spin precession in an electric field. To reduce the sensitivity to the larger spin precession caused by magnetic fields, we compare the ^{199}Hg Larmor precession frequencies in two adjacent cells having equal but oppositely directed electric fields applied parallel to a common magnetic field. Magnetic field shifts common to the two cells cancel, leaving the system magnetically sensitive only to changes in the magnetic field gradient. From Eq. (1), an EDM would cause a frequency shift of $2\,Ed/h$ in each cell. The magnitude of the EDM is given by

$$d=\frac{h}{4E}\,\delta\nu, \tag{2}$$

where $\delta\nu$ is the difference between the spin precession frequencies of the atoms in the two cells and h is Planck's constant. To extract d, we measure the change in $\delta\nu$ as **E** in each cell is reversed.

HG2 has four major improvements over HG1: incorporation of a transverse pumping scheme, which eliminates frequency shifts due to the pump light; stabilization of the Hg density and the spin relaxation time of the optical pumping cells; elimination of the most serious magnetic perturbation by reducing the leakage currents across the cells to the pA level; and an increase in signal by using enriched ^{199}Hg rather than natural Hg in the cells. These improvements as well as other changes are discussed in the following two sections.

The measurement is now sensitive to frequency shifts on the order of 2 nHz, the smallest energy shift that has ever been detected in any experiment. This sensitivity allows us to set the smallest limit to date for the EDM of any system.

II. TRANSVERSE SYNCHRONOUS OPTICAL PUMPING

In HG1, the statistical uncertainty in measuring a precession frequency shift was dominated by noise on the light intensity. This noise produced fluctuations in precession frequency through the virtual light shift [15], a shift in the ground state Zeeman energy splitting brought about in this case by the circularly polarized pumping light. Because of the optical selection rules on the magnetic quantum number m_I, the electric vector of circularly polarized light induces unequal ac Stark shifts for the two values of m_I along the propagation direction of the light, causing an effective ground state Zeeman splitting.

In HG2, this serious light-shift problem is avoided by using transverse optical pumping, in which the magnetic field is perpendicular to the light propagation direction. A synchronous pumping scheme is used to continually pump the ground state spin polarization as it rotates in the magnetic field. Early work with transverse pumping schemes used modulated intensity [16], but in our case we modulate instead the circular polarization of the light by passing plane-polarized light through a rotating quarter-wave plate. When the frequency of modulation of the circular polarization is close to the Larmor precession frequency of the nuclear spins, the nuclear-spin polarization builds up and in turn

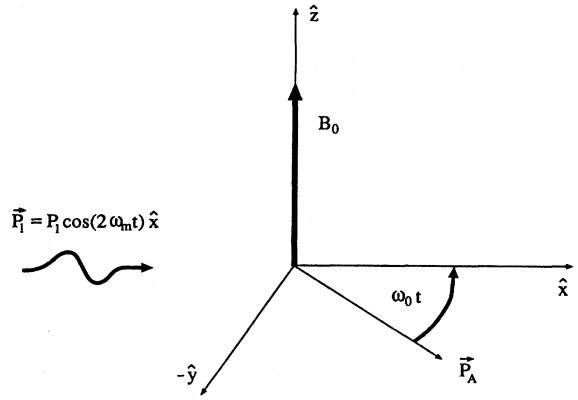

FIG. 1. Transverse pumping geometry.

modulates the transmitted light intensity. Thus, the precession of the nuclear-spin polarization can easily be monitored and its frequency measured with a high signal-to-noise ratio.

This transverse pumping scheme reduces the virtual light shift by approximately a factor of 300 over our previous experimental setup not only because the magnetic field is now perpendicular to the light propagation direction, but also because the polarization of the light averages to near zero (0.5%) over one precession cycle. In the present system, the statistical noise is limited by shot noise on the light detected by the photomultipliers. A characterization of the noise in the system can be found in Appendix A.

The geometry of the system is given in Fig. 1. The pump light, traveling in the $\hat{\mathbf{x}}$ direction, passes through a linear polarizer with polarization axis along $\hat{\mathbf{y}}$, through a quarter-wave plate with its retardation axis rotating counterclockwise with an angular velocity ω_m, then through the atomic vapor in the presence of the magnetic field ($B_0\ \hat{\mathbf{z}}$), and into a photomultiplier where it is detected.

The spin-$\frac{1}{2}$ ^{199}Hg nuclei can be modeled as an ensemble of classical magnetic moments precessing in the presence of the pumping light and the magnetic field. For incident intensity I_o (considering only resonant light), the light transmitted through the vapor $[I(t)]$ is

$$I(t)=I_o\exp\{-\alpha[1-\mathbf{P}_l(t)\cdot\mathbf{P}_A(t)]\}, \tag{3}$$

where α is the optical depth (number of absorption lengths) of the vapor, $\mathbf{P}_l(t)=P_l(t)\ \hat{\mathbf{x}}$ is the time-dependent circular polarization of the light along the propagation direction, and $\mathbf{P}_A(t)$ is the atomic (i.e., nuclear-spin) polarization.

To specify $P_l(t)$, we take the optical electric field axis of the $\lambda/4$ plate to lie along the $\hat{\mathbf{y}}$ axis at $t=0$ and to be rotating counterclockwise as viewed along $\hat{\mathbf{x}}$. Using the Jones vector notation [17] for the components of the unit optical electric field $\hat{\mathbf{e}}$, we find

$$\begin{pmatrix} e_y \\ e_z \end{pmatrix}=\begin{pmatrix} i\sin(2\omega_m t) \\ 1-i\cos(2\omega_m t) \end{pmatrix}, \tag{4}$$

where we have set the overall phase factor equal to one. $P_l(t)$ can be found by converting to the circular polarization basis,

$$\begin{pmatrix} e_+ \\ e_- \end{pmatrix} = \frac{1}{2}\begin{pmatrix} +\cos(2\omega_m t)+i[1+\sin(2\omega_m t)] \\ -\cos(2\omega_m t)-i[1-\sin(2\omega_m t)] \end{pmatrix}, \quad (5)$$

whence

$$\mathbf{P}_l(t) \equiv (e_+^2 - e_-^2)\hat{\mathbf{k}} = \sin(2\omega_m t)\hat{\mathbf{x}}. \quad (6)$$

The atomic polarization evolves as

$$\left(\frac{d\mathbf{P}_A}{dt}\right) = -\gamma \mathbf{P}_A \times \mathbf{B}_o + \Gamma_p(\mathbf{P}_l - \mathbf{P}_A) - \Gamma_r \mathbf{P}_A, \quad (7)$$

where Γ_p is the rate at which unpolarized atoms absorb the light, Γ_r is the rate at which atoms are depolarized by collisions with the walls of the cell, and γ is the gyromagnetic ratio of the individual atoms determining their precession rate in the magnetic field B_o. Using the geometry of Fig. 1 and the expression for $\mathbf{P}_l$ above leads to

$$\left(\frac{d\mathbf{P}_A}{dt}\right) = -\omega_L \mathbf{P}_A \times \hat{\mathbf{z}} - \Gamma \mathbf{P}_A + \Gamma_p \sin(2\omega_m t)\ \hat{\mathbf{x}}, \quad (8)$$

where $\omega_L = \gamma B_o$ is the Larmor precession frequency of the atoms and $\Gamma = \Gamma_p + \Gamma_r$.

This equation can be solved by transforming into a reference frame rotating at a frequency $2\omega_m$ about $\hat{\mathbf{z}}$ in the same direction as the atoms are precessing. The time derivative of the atomic polarization vector becomes

$$\left(\frac{d\mathbf{P}_A}{dt}\right)_{\text{rot}} = \left(\frac{d\mathbf{P}_A}{dt}\right) - 2\boldsymbol{\omega}_m \hat{\mathbf{z}} \times \mathbf{P}_A \quad (9)$$

$$= -\Delta\omega \mathbf{P}_A \times \hat{\mathbf{z}} - \Gamma \mathbf{P}_A + \Gamma_p \sin(2\omega_m t)\ \hat{\mathbf{x}}, \quad (10)$$

where the subscript "rot" refers to the derivative in the rotating frame and $\Delta\omega = \omega_L - 2\omega_m$. Since $\gamma > 0$ for ^{199}Hg, the transformation matrix to be used on the right-hand side of this equation is

$$R = \begin{pmatrix} +\cos(2\omega_m t) & -\sin(2\omega_m t) & 0 \\ +\sin(2\omega_m t) & +\cos(2\omega_m t) & 0 \\ 0 & 0 & 1 \end{pmatrix}. \quad (11)$$

Because $2\omega_m/2\pi \gg \Gamma_p$, the oscillating terms in the rotating frame can be averaged (the secular approximation), giving

$$\left(\frac{d\mathbf{P}_A}{dt}\right)_{\text{rot}} = (-\Delta\omega \mathbf{P}_A \times \hat{\mathbf{z}} - \Gamma \mathbf{P}_A + \tfrac{1}{2}\Gamma_p\ \hat{\mathbf{y}})_{\text{rot}}. \quad (12)$$

The steady-state solution is obtained by setting the rate of change of each component of the atomic polarization equal to zero. Solving these equations gives

$$(\mathbf{P}_A)_{\text{rot}} = \frac{\Gamma_p}{2(\Gamma^2 + \Delta\omega^2)}\begin{pmatrix} -\Delta\omega \\ \Gamma \\ 0 \end{pmatrix}. \quad (13)$$

Rotating back into the laboratory frame, the atomic polarization is

$$\mathbf{P}_A = \frac{\Gamma_p}{2(\Gamma^2 + \Delta\omega^2)}\begin{pmatrix} -\Delta\omega\cos(2\omega_m t) + \Gamma\sin(2\omega_m t) \\ +\Delta\omega\sin(2\omega_m t) + \Gamma\cos(2\omega_m t) \\ 0 \end{pmatrix} \quad (14)$$

and

$$\mathbf{P}_l \cdot \mathbf{P}_A = \frac{\Gamma_p \Gamma}{4(\Gamma^2 + \Delta\omega^2)}\left[1 - \cos(4\omega_m t) - \frac{\Delta\omega}{\Gamma}\sin(4\omega_m t)\right]. \quad (15)$$

Note that the modulation of the transmitted light intensity is at $4\omega_m$. This is clear from Eq. (3) since both P_l and P_A vary in time at 2ω, and thus the product varies at 4ω. The second term in Eq. (15) is the component of the atomic polarization, which is in phase with the light polarization and has an "absorption" line shape, while the third term is the portion that is 90° out of phase with the light polarization and has a "dispersive" line shape. The phase angle between P_A and P_l near resonance is

$$\tan\phi \approx \phi = \frac{\Delta\omega}{\Gamma}. \quad (16)$$

The sensitivity of the system to a change in $\Delta\omega$ (brought about, for example, by a shift in precession frequency of the atoms) in terms of the in-phase (V^{in}) and out-of-phase (V^{out}) voltages from lock-in amplifiers referenced by $\cos(4\omega_m t)$ is

$$\frac{dV^{\text{out}}}{d(\Delta\omega)} = \frac{V^{\text{in}}}{\Gamma}, \quad (17)$$

where we have taken $\phi = V^{\text{out}}/V^{\text{in}}$.

Under optimum operating conditions $\Gamma_p \approx 3\Gamma_r$ (for maximum sensitivity), and the oscillators are approximately on resonance ($\Delta\omega = 0$). In practice, it is difficult to achieve this high pump rate, but the maximum is a broad one. Typically we run with $\Gamma_p = 2\Gamma_r$, which reduces the sensitivity only by 3%. Making this substitution in Eq. (15), Eq. (3) takes the form

$$I(t) = I_o \exp\left\{-\frac{\alpha}{6}[5 + \cos(4\omega_m t)]\right\}. \quad (18)$$

Our mercury EDM cells typically have about one optical depth $\alpha = 1$. We measure a *modulation* "depth" on the transmitted light of 15–20 %, which is consistent with Eq. (18) if the nonresonant light (about 20% of the incident light) is included.

III. EXPERIMENTAL APPARATUS

Figure 2 is a schematic overview of the apparatus. Diverging resonance radiation from the ^{204}Hg microwave (electrodeless) discharge lamp is collimated by a converging lens, travels along $\hat{\mathbf{x}}$, and encounters a plane polarizer oriented either along the $\hat{\mathbf{z}}$ or $\hat{\mathbf{y}}$ direction. The 254-nm resonance radiation then passes through a quarter-wave plate,

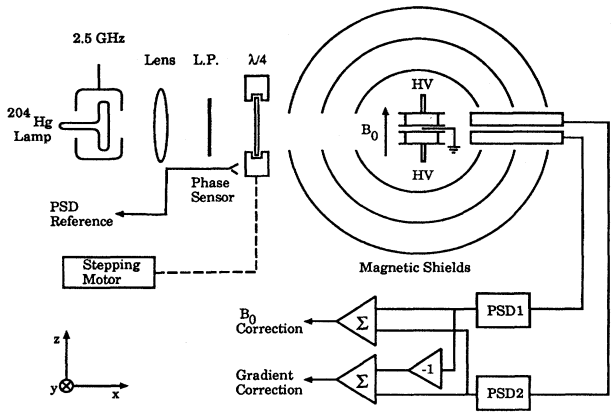

FIG. 2. ^{199}Hg EDM experiment block diagram.

which is rotating in the y-z plane at a constant frequency, ω_m, which is one-half the precession frequency of the ^{199}Hg spins. The quarter-wave plate is rotated by a stepping motor driven by a signal derived from a crystal oscillator. On the perimeter of the quarter-wave plate is a slotted wheel with a lamp and detector scheme to provide a reference frequency for the phase detectors. The linear polarizer and quarter-wave plate combination modulate the circular polarization of the light at $2\omega_m$. The light then enters the three layer magnetic shields, where the vapor cells are located in the presence of a static magnetic field $B_0\hat{\mathbf{z}}$ and an electric field $\mathbf{E}$ applied parallel to $\mathbf{B}$, which is equal in magnitude but opposite in direction in the two cells. The electric field is produced by a 0–15-kV power supply and the leakage currents across the cells and to the cell holding vessel are monitored with three separate current monitors. The cells contain about one absorption length of ^{199}Hg vapor.

To the extent that the Larmor precession frequency is equal to the light polarization modulation frequency, the atoms in the cell will attain a steady-state polarization, which precesses about B_0, and the transmitted light will acquire an intensity modulation at $4\omega_m$ (see Sec. II). The light transmitted through each cell is detected separately; the signals are amplified and fed into two sets of phase sensitive detectors (PSD's). Each set has two PSD's, one for the component of the transmitted light, which is in phase with the light polarization ($V_1^{\rm in}, V_2^{\rm in}$), and one for the component that is 90° out of phase with the light polarization ($V_1^{\rm out}, V_2^{\rm out}$). When $2\omega_m \approx \omega_L$, $V_1^{\rm out}$ and $V_2^{\rm out}$ are approximately linear in $\Delta\omega$ [see Eq. (16)], so we use their sum in a feedback loop to stabilize B_0 (i.e., the loop sets B_0 such that $V_1^{\rm out}+V_2^{\rm out}=0$).

In addition to the B_0 field, we also have a set of "anti-Helmholtz" coils to produce a magnetic field gradient between the two cells. This coil has a dual purpose. First, we use it to null any magnetic field offset that exists between the cells. This offset may drift during the course of a data run, so we feed back the difference between $V_1^{\rm out}$ and $V_2^{\rm out}$ to set the gradient correction in this coil (i.e., the gradient coil current is set such that $V_1^{\rm out}-V_2^{\rm out}=0$). Second, because the electric field is oppositely directed in the two cells, an EDM would produce an asymmetric shift in frequency between the two cells, and the gradient feedback loop would null this shift. An EDM would be manifest by a change in the gradient correction signal correlated with the application of high voltage.

With both the B_0 and gradient coil feedback loops in operation, the atomic oscillators are locked to $V_1^{\rm out}=V_2^{\rm out}=0$. From Eqs. (15) and (16), this leads to the condition that for each oscillator,

$$\left(\frac{|\omega_L|-|2\omega_m|}{\Gamma_p+\Gamma_r}\right)+\phi_{\rm offset}=0, \tag{19}$$

where $\phi_{\rm offset}$ is the phase offset between the actual light polarization and the reference signal to the phase sensitive detector. Electronic phase shifts and imperfect optics can make $\phi_{\rm offset}$ slightly different for the two oscillators. From Eq. (19) it is apparent that were the light intensity to vary, Γ_p, which is proportional to the light intensity, would also change. If $\phi_{\rm offset}$ is not zero, then the feedback loops would cause ω_L to change to satisfy Eq. (19). We set $\phi_{\rm offset}$ to zero for each oscillator by reducing the light intensity by a factor of 2 (using a screen in the light path) and adjusting the reference signal phases so that the correction signals from the feedback loops do not change with the change in light intensity (i.e., ω_L remains constant). The phase offset between the two cells was a reproducible function of linear polarizer orientation and rotation direction of the quarter-wave plate and was corrected by shifting the reference signal to one of the cells by 0–500 μs (0–4.3 mrad). For the earliest data reported here (data sets 1 and 2), only the B_0 feedback loop was made insensitive to changes in the light intensity. This forces only the average $\phi_{\rm offset}$ for the two oscillators to zero. For all subsequent data, both loops were made insensitive to the light intensity, forcing $\phi_{\rm offset}$ to zero for both oscillators.

In the following sections, we describe each portion of the apparatus in detail.

A. Light source

The ^{204}Hg discharge lamp bulbs that provide the resonant light are fabricated as described in [18,19]. The bulb consists of a quartz cylinder measuring 14 mm in diameter and 5 mm in length, with a centered stem attached to the back and a quartz disk attached to the front. The lamp stem is held in a copper cylinder with its temperature regulated by a thermal servo circuit. Each lamp contains approximately 1 mg of enriched ^{204}Hg and 3 torr of argon and lasts for about 1000 h of use. Light from these lamps has a Doppler-broadened linewidth of 2 GHz and a center frequency approximately 1.5 GHz to the red of the pressure-shifted 3-GHz-wide ^{199}Hg absorption line.

The lamp driver consists of a cylindrical resonating cavity (gold plated copper), driven with a microwave-oven magnetron at 2.455 GHz. The magnetron requires a 3.14-V dc-regulated (1%) filament supply, which can deliver 14 A and "floats" at the anode voltage of −3500-V dc. The anode current is about 15 mA. A detailed description of the design and construction of the lamp driver and current regulation is given in Ref. [18].

B. Light polarization and modulation

During data sets 1 and 2, we used a rotating linear polarizer followed by a fixed quarter-wave plate to produce the

modulated polarization described in Sec. II. The linear polarizer was a polymer film far UV-visible linear polarizer sold by Oriel. The transmission is about 20% when new, but degrades significantly when exposed to the UV light. For this reason, in the last three data sets we polarized the light by reflection off of a stack of three quartz plates set at the Brewster angle. Incoming unpolarized light reflects off of three successive mirrors and then the Brewster plate, all mounted on a rotating platform with the angles of the mirrors set so that we can rotate the axis of linear polarization without redirecting the beam path. This provides better polarization and slightly better "transmission" than the film polarizer but the polarization cannot be rotated at the required frequency, so in data sets 3–5 we fix this linear polarizer and rotate the quarter-wave plate instead.

The quarter-wave plate is rotated using a stepping motor in the 400 step per revolution mode at $\omega = 2\pi \times 4.3$ rad/s. The shaft of the motor couples to an aluminum disk, which rotates freely in a ring ball bearing assembly. A 6-in.-diameter browning gear is mounted symmetrically on the aluminum disk. Next to the first gear is an identical gear mounted in the same way, with the quarter-wave plate positioned at the center. Our quarter-wave plate is a 1.5-in.-diameter zero-order optically contacted quartz disk, chosen for its low sensitivity to temperature fluctuations and large acceptance angle.

On the perimeter of the second gear there is a slotted wheel (16 slots) with a fixed small lamp and detector mounted on either side. This produces a 16 pulse per revolution signal which, when divided by two, provides a symmetric square-wave reference at eight times the rotation frequency for the phase sensitive detectors. A second lamp and detector scheme with a single flag aligned with the fast axis of the quarter-wave plate is used to synchronize the reference signal with the light polarization.

C. Magnetic shields

The magnetic shields used for this experiment are three concentric cylinders made of molypermalloy, each with two endcaps. The cylinders have lengths of 51, 69, and 107 cm, and radii of 9.5, 11.5, and 24.0 cm. Each cylinder has two 1-in. holes cut in the center on opposite sides to allow light to pass through. The cylinders are mounted concentrically, with the holes aligned, using wooden rings spaced symmetrically along the length and held in place with silicone glue. This gives maximum support without inducing stresses or strains in the shields. The shields are held securely on a wooden platform, which is set along with the optics on a 3-in.-thick aluminum slab resting on a 3-ft. layer of styrofoam. The styrofoam in turn rests on a concrete slab that is vibrationally isolated from the building.

The transverse shielding factor of the set of magnetic shields after assembly was measured to be $67\,000 \pm 6000$. Stresses and strains in the molypermalloy, as well as temperature gradients, can greatly reduce both the stability and the shielding factor of the shields. We used a "degaussing" (demagnetizing) procedure that greatly reduced both the daily drift and number of discreet "jumps" in the field gradient. When properly degaussed, the drift in magnetic field gradient across the cells was typically less than 1 nG/h. The degaussing procedure is as follows. After any B_0 field reversals, or after the shields have been disturbed in any other way, a 60-Hz current is run through a coil, which passes through the center of the shields (longitudinally), and around the outside. The current is slowly increased until the shields saturate at which time each of the three shields is tapped firmly on the endcaps. The current is then slowly reduced to zero and the power is disconnected with a bounceless switch; each of the endcaps is tapped firmly again.

D. Magnetic field generation and stabilization

The static, uniform magnetic field B_0 is generated by a 15 turn coil wound onto a nylon cylindrical form in a cosine distribution inside of the innermost magnetic shield. The calibration of the coil, measured experimentally, was found to be 2.0 μG/μA. We also measured the field gradient across the cells produced by a change in B_0 and found that it was approximately one part in 10^4 of B_0, which is a major portion of the total field gradient inside the shields.

The B_0 coil current was derived from a trickle-charged 12-V battery; a 6-V Hg—Cd reference cell was used to maintain a constant voltage drop across a precision wire-wound resistor in series with the B_0 coil.

In addition to the B_0 windings, there are two turns of wire in an anti-Helmholtz configuration, producing a field gradient between the cells. The gradient field was measured directly and found to be 14 nG/(μA cm). This measurement was verified by direct calculation. The separation of the vapor cell centers is 1.3 cm, which gives about 15-μHz/μA frequency shift between the cells. A second anti-Helmholtz coil is attached to the cell holding vessel. These coils were used in the gradient coil feedback loop, mentioned above and described in detail in Ref. [18], which forces the difference between the out-of-phase signals from the atomic oscillators to zero. The gradient feedback coil can be calibrated conveniently by passing a known current through the first gradient coil and measuring the change in gradient correction voltage. With a 1-MΩ resistor in series with the feedback coil, the calibration is 26 μHz/V.

E. Optical pumping cells

The Hg vapor cells used in this experiment required an extensive development phase to satisfy the requirements of having a long spin-relaxation time and stable Hg density while containing electrodes for application of the high voltage (HV) and having leakage current of $\sim$ 0.1 pA/kV. While we continue to work on developing better cells, these cells represent a major improvement over previous cells. The technique for making our current cells is described in Appendix B.

The main cylinder, endplates, and fill stem of the cells are made of high-purity, synthetically produced fused silica (Heraeus Amersil Suprasil I). The cell body is made from 25.0-mm i.d.$\times$ 27.5-mm o.d. tubing and is 10 mm long; a fill stem attached to this cylinder is made of 2.4-mm i.d. tubing, which has been drawn to an i.d. of 1 mm. The endplates are 1.5-in. diam$\times$1/16-in.-thick ground and polished disks.

The inner surface of the cell endplates are coated with tin-oxide (SnO_2) to provide a conductive surface for the application of the electric fields, and the body of the cell is

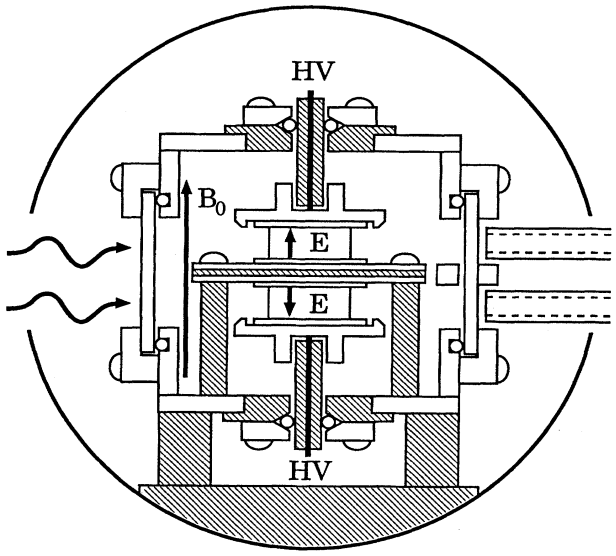

FIG. 3. Cell-holding vessel for the EDM cells. Insulators are crosshatched. Outer circle shows relative size of the inner surface of the magnetic field windings form.

dipped in a siliconizing agent to make the surfaces nonwettable and increase the spin-relaxation time. The endplates are then glued onto the cell body using Varian Torr-Seal. A thin coating of wax (dotriacontane) keeps the Hg from sticking to the electrodes but must be cleaned off of the cell body to keep the leakage currents low. Getting this wax coating just right is the key to achieving long lifetimes and low leakage currents.

The cells contain approximately one absorption length of isotopically enriched (95%) metallic ^{199}Hg and 300 torr of buffer gas that is 95% N_2 and 5% CO.

Cells prepared in this way have an initial limiting spin-relaxation lifetime of 45 s. Over a period of several thousand hours exposure to UV light, the lifetimes would degrade to 20 s. Subsequent redistribution of the wax gave lifetimes of up to 90 s, and lifetimes of up to 70 s have been stable over 5000 h of exposure to UV light.

F. Cell-holding vessel

The EDM cells are held in place inside of an air-tight aluminum vessel designed to minimize systematic errors that can arise from magnetic fields of both charging (displacement) currents and steady-state leakage currents. Figure 3 shows the roughly cubicle vessel in cross section. The circle enclosing the vessel shows the relative size of the inner surface of the nylon form on which the B_0 field coils are wound. The light enters through a quartz window mounted with as little stress as possible; stress birefringence not only can cause the two cells to see slightly different light polarization, but this difference can be affected substantially by temperature and pressure changes.

The top cell rests on its square ground plane, which is supported at the corners by four Lucite rods. Above the cell is an aluminum electrode that is held in place by the high-voltage feedthrough, which consists of a quartz tube with a tinned copper wire running down the center. The tube passes through an aluminum disk, secured to a Lucite disk. When the cell is in place, the aluminum disk is tightened down, pressing an "O" ring against the tube and holding it in place. The bottom cell is secured from the bottom by its HV feedthrough in the same way. Each cell has its own ground plane, insulated from the main vessel by the Lucite rods; a mylar sheet separates the ground planes for the two cells.

The ground return wires (four for each cell) are attached at the corners of the ground plane and exit the vessel at the top (bottom) for cell two (one). The wires for each cell then converge (through 100-Ω resistors to equalize the current) and follow the high-voltage leads back to the supply where they are measured using the current followers described in Sec. IIIH. To reduce the leakage currents, the vessel is filled with freon, purged daily, which not only inhibits electrical discharge, but also serves as a cleaning and drying agent for the inner surfaces of the vessel.

G. Light detection

The light is detected by two Hamamatsu solar-blind transmission-type photomultiplier tubes (R759). The tubes have a 1-cm-diameter Cs—Te photocathode with a 10% quantum efficiency and a radiant sensitivity of 20 mA/W at 254 nm. To avoid saturation, the photocurrent is extracted from the fifth dynode (out of ten), with the unused dynodes held at a bias voltage of 7 V. The dark current in this configuration is a few pA at most.

The light transmitted through each cell is collected separately by a nonreflecting tube 5 in. long and adjacent to the cell holding vessel. Reflecting tubes collected only slightly more light and were found to have polarization-dependent transmission, giving background signals on the detected light at the atomic signal frequency due to rotation of the wave plate. This constraint also prevented us from using side-on photomultiplier tubes, which have twice the quantum efficiency but were found to have a polarization-dependent sensitivity.

H. Detection electronics

The typical anode current from the photomultipliers is 300 nA and is monitored by a current-to-voltage converter. The dc part is filtered out with a 0.1-Hz-high pass filter and amplified. The signal from the slotted wheel is a square wave at twice the frequency of light modulation. This signal is fed into two digital $\div 2$ circuits, generating four square waves shifted in phase from each other by 90°.

The PSD consists of four switches and an operational amplifier arranged such that the gain of the amplifier can be switched between $+1$ and -1 at the reference frequency. This is followed by a three-pole active low-pass filter with cutoff frequency of 1 Hz. The operational amplifiers used for this circuit are super chopper stabilized (Intersil ICL7650S), which were chosen for their excellent stability and small input offset voltages. The dynamic rejection ratio of these PSD's, defined by $20 \log_{10}(\Delta V_{\text{out}}/\Delta V_{\text{in}})$dB, was better than -60 dB. Details of this circuit can be found in [18].

The leakage current monitors use precision low-power high-impedance input electrometer op amps made by Analog Devices (AD549K). The circuit is a simple current follower, but we use a resistor "T network" to achieve high

TABLE I. Distinguishing features of the data sets. The prime in the cell orientation column indicates that a cell was turned upside down. $\bar{\nu}$and $\delta\nu$ refer to the B_0 and gradient coil feedback signals, respectively. After data set 2, cells 3 and 4 became unusable.

Data set	No. runs	Hg cells and orientation	Rotating optical component	PSD phase set by	Applied E (kV/cm)
1	54	1 over 2	Polarizer	$\bar{\nu}$	5 and 10
2	100	3 over 4	Polarizer	$\bar{\nu}$	5 and 10
3	48	1 over 2	λ/4 plate	$\bar{\nu}$and $\delta\nu$	5 and 10
4	49	2 over 1	λ/4 plate	$\bar{\nu}$and $\delta\nu$	5 and 10
5	48	1 over 2′	λ/4 plate	$\bar{\nu}$and $\delta\nu$	7

sensitivity (≈21 mV/pA) without the need for excessively high resistor values.

The data taking computer is an IBM clone equipped with two IBM input/output (I/O) boards, each of which has a four channel analog-to-digital converter and a 16-bit parallel port output. One of the I/O boards was used exclusively for signals related to the high voltage in order to avoid crosstalk between the HV and the other data channels. These signals include four inputs, (the three leakage current monitors, and the high-voltage monitor) and three outputs. (The HV ± and on-off control voltages and a HV multiplexer that connects the HV signals to the computer only when they are being read.) The rest of the channels, which are not associated with the high voltage, are monitored using the other I/O board and a separate multiplexer.

I. High-voltage supply

Both the high-voltage supply and the leakage current monitors are about 3 m away from the data acquisition system and the magnetic shields. The high-voltage cable is enclosed in a tinned copper wire braid to keep the surface from charging up. The leakage to the braid is about 0.6 pA/(kV m). The cable, which carries the leakage currents, is shielded coax. It runs from the shields to the HV supply along the same path as the HV wire to minimize any current loops, which could produce magnetic fields associated with the high voltage.

The high-voltage power supply has a range of 0–15 kV and can be remotely programmed for both on-off and plus-minus operation. It is generated by driving a 60-Hz high-voltage transformer with a variable-amplitude 2-kHz (resonant) square wave. The transformer output is rectified, filtered, and connected to the vapor cells. To stabilize the voltage, the output of the high-voltage supply is divided down to 0.5 V/kV and compared to a set point. The comparator produces an error signal, which is integrated and fed back to the 2-kHz square-wave generator. Two push-type solenoids switch the polarity by reversing the connection of the HV contacts to the floating supply. Short-term stability of the high-voltage supply is very important because fluctuations in the high voltage produce sizable variations in leakage currents.

IV. DATA ACQUISITION AND ANALYSIS

A. Acquisition

The data we report here consist of 299 24-h data runs taken over a period of three years. We divide the data runs into five chronologically ordered data sets, where each data set includes a series of consecutive runs that use a specific pair of Hg vapor cells in a fixed orientation. Between data sets, modifications and improvements to the experimental apparatus were made. Table I lists the major distinguishing features of the data sets.

The first reported results [7] of HG2 included data sets 1, 2, and 3 only; data sets 4 and 5 were taken since then. In addition, we have discarded the first 34 runs of data set 1 (which were included in [7]). During these runs the high-voltage supply was unstable on one polarity, giving a large atomic frequency shift that was quadratic in the applied electric field (an EDM would be linear in **E**). By discarding these runs, the results we report here have all been taken with the rebuilt voltage supply and show essentially no atomic signals quadratic in **E**. The inclusion of these runs would not change our current EDM results, as the omitted runs carry little statistical weight and showed no signals linear in **E**.

Between one-day runs, we changed experimental parameters including (in order of decreasing frequency of change) the sign of the gradient feedback current, the value of the applied high voltage (data sets 1–4 only), the direction of rotation of the light polarization modulator, the angle of the fixed optical component (either 0° or 90°), and the sign of the precession field B_0. The sequence of parameter changes followed orthogonal Walsh functions [20].

A true EDM signal should be linear in the applied voltage and independent of any of the parameter changes apart from the gradient feedback current. Reversing this current changes the sign of the experimental signal for a true EDM: if one orientation of **E** field in the cells required a positive correction voltage to the gradient coil to keep the two vapor cells in phase, then, after reversing the gradient coil feedback connection, a negative correction voltage would be required. This reversal allowed us to distinguish a true EDM signal from a variety of electronic pickup or crosstalk effects that might be caused by reversal of the high voltage.

For each data run, the voltage applied across the vapor cells followed the sequence [+HV, 0, −HV, 0], where HV was either 5, 7, or 10 kV for the entire run. Each voltage dwell lasted 250 s except for alternating runs in data sets 1 and 2 for which the voltage dwells were shortened to 210 s. Throughout the entire voltage sequence, data were taken continuously: every 0.1 s the signals from 16 data channels were digitized and read by a computer. Each consecutive 50 s of data was averaged to a single point and converted to physical units. The data analysis was subsequently performed on these averaged readings, giving five time segments per voltage dwell (four segments for half of the runs in

data sets 1 and 2). The voltage was ramped linearly to its final value in the first 70 s of the voltage dwell. Resultant displacement currents that flowed across the vapor cells subsequently decayed with a 10-s time constant and the atomic oscillators relaxed from the perturbations induced by the ramping currents with a 20-s time constant. We analyzed the first 150 s of the voltage dwells to monitor the effects of the voltage ramp on our signals; the data taken after 150 s was used to extract the steady-state behavior of our system.

The 16 data channels that were monitored continuously include $\delta\nu$, the error signal from the gradient coil feedback loop; $\bar{\nu}$, the error signal from the **B** feedback loop; V_1^{in}, V_2^{in}, V_1^{out}, and V_2^{out}, the outputs of the PSD's discussed in Sec. IIIH; $\mathscr{T}_1$ and $\mathscr{T}_2$, the average light intensity measured by each photomultiplier; $\mathscr{T}_{\text{mon}}$, the light intensity measured at the lamp output; HV, the output of the high-voltage supply; the divided down output of the HV supply; $\mathbf{T}_L$, the stem temperature of the discharge lamp; B_{amb}, the component of the ambient magnetic field outside of the magnetic shields parallel to **B** as measured by a flux gate magnetometer; and i_1, i_2, and i_m, the leakage currents across the two vapor cells and to the vessel that holds the cells. Plots of the raw data for selected channels are shown for a typical data run in Fig. 4. Figure 5 shows a Fourier transform of the averaged data for $\delta\nu$ channel.

B. Analysis

The signature of an EDM is a frequency shift linear in **E** between the two vapor cells, as measured by the gradient coil feedback channel, $\delta\nu(\mathbf{E})\equiv\frac{1}{2}[\delta\nu(V_{\text{HV}}+)-\delta\nu(V_{\text{HV}}-)]$. We also extract signals proportional to $|E|$, $\delta\nu(|E|)\equiv\delta\nu(V_{\text{HV}}=\text{on})-\delta\nu(V_{\text{HV}}=\text{off})$, as might be caused by the magnetic field of leakage currents that flow parallel to **B** or Stark shifts. A large frequency shift proportional to $|E|$ along with imperfect reversals of **E** could lead to a systematic error that appears to be linear in **E**. Finally, to examine the possibility that the displacement currents from the high-voltage ramp might magnetize the magnetic shields, or that magnetic fields generated by the high-voltage supply switches might be shielded imperfectly, we also examine the voltage dwells for which no voltage is applied. Specifically, we treat the0 voltage dwell after the +HV dwell as a 0^+ dwell and that after the −HV dwell as a 0^- dwell, and extract a pseudo-EDM signal proportional to 0^+-0^-, $\delta\nu(0)\equiv\frac{1}{2}[\delta\nu(0^+)-\delta\nu(0^-)]$.

The analysis must extract such signals in the presence of a drifting background that contains occasional discrete jumps. First- and second-order drifts in time were subtracted off using either an overlapping weighted string, or a fit to a second-order polynomial in time. If $\{x_i\}$ represents a set of points that follow the HV sequence $\{V_{\text{HV}}^+,0^+,V_{\text{HV}}^-,0^-\}$, then the string points for the signal proportional to **E** are given by

$$y_i=(-1)^{i+1}[x_{2i-1}-3x_{2i+1}+3x_{2i+3}-x_{2i+5}]/8, \quad (20)$$

and similarly for the 0^+-0^- and $|E|$ signals. The mean and standard deviation of these string points was calculated to determine a single result for each run; the standard deviation was multiplied by $(16/5)^{1/2}$ to correct for the correlation between the string points. Removing these drifts has little effect on the central value of an EDM but allows for an estimate of the uncertainty in the measurements as the electric field is reversed over the course of a data run. Three different methods of subtracting off the backgrounds gave final EDM results consistent at the level of $\frac{1}{5}\sigma_{\text{stat}}$.

Two independent analyses were performed to extract signals proportional to E, $|E|$, and 0^+-0^- after removing the drifting background; the two differed in the method used for removing jumps in the data.

The first analysis identifies jumps in one channel at a time by comparing the difference between successive HV dwell points (separated by 500 s) for each 50-s segment of each channel to the error bar for these points. A cut is made in that channel if

$$|x_i-x_j|>\eta[\sigma_i^2+\sigma_j^2]^{1/2}, \quad (21)$$

where i and j denote any adjacent pair of HV dwell points, and $\sigma_{i,j}$ is an average error bar of a point. For the $\delta\nu$ channel we used $\eta=3$, which on average discarded less than 3% of the data. Increasing η by a factor of 3 throws out less than 0.3% of the points and changes the final EDM result by less than $\frac{1}{7}\sigma_{\text{stat}}$.

The second analysis identifies jumps by looking for a discontinuity in the first derivative of $\delta\nu$, $\bar{\nu}$, V_1^{in}, V_2^{in}, $\mathscr{T}_1$, $\mathscr{T}_2$, or B_{amb}. If any pair of derivatives, 100 s apart, are found to differ by more than three times the standard deviation for that channel over the entire run, then the data is cut from all channels. On average, this analysis threw out 7% of the data, mostly from jumps seen on the fluxgate magnetometer, B_{amb}.

For each data set, by HV value and for each 50-s time segment, we computed the mean and standard deviation of the individual run results to find a single result for each segment. (We also compute the inverse-error-squared weighted error bar for each set and take the larger of the two uncertainties as the uncertainty for a set.) Dividing each result by the HV value gives the sensitivity to an EDM; a weighted average of these results gives our final results for each channel.

The two analyses give final results that differ by only $\frac{1}{5}\sigma_{\text{stat}}$. The results in the tables that follow reflect the results of the second analysis described above. Our final result reflects the average of the two analyses.

Table II shows the signals from each data set for the $\delta\nu$ channel. The values shown are the averages of the last two time segments, beginning 150 s into the voltage dwell, for which the signals have reached their steady-state values. The last three rows in Table II show the combined results for 7, 5, and 10 kV.

Table III shows the results for $\delta\nu$ for all time segments, where time segment j is the jth 50-s interval of the voltage dwell. As seen in Table III, there is evidence for a frequency shift due to HV ramp displacement currents in some of our data: In the first time segment, the **E** and 0^+-0^- signals show opposite shifts as would arise from currents ramping up and then down. We are confident that the effects of the displacement current perturbation have decayed away by the fourth time segment.

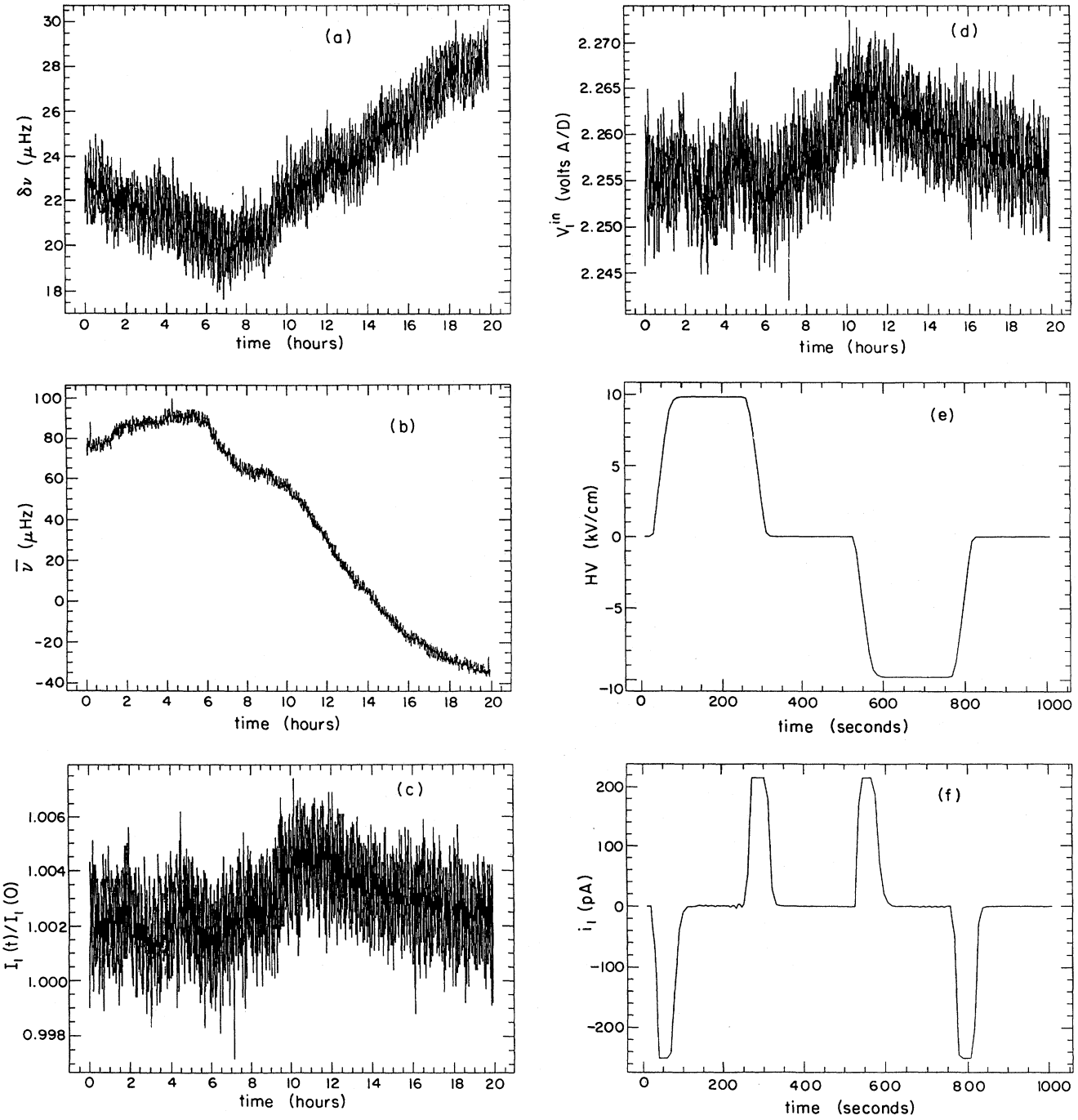

FIG. 4. Raw data for selected channels for a typical run. (a) $\delta\nu$, the frequency difference between the two cells; (b) $\bar{\nu}$, the average precession frequency in the two cells; (c) the normalized light intensity transmitted through cell 1; (d) the portion of the detected light intensity in phase with the light polarization; (e) the divided down HV for a single reversal sequence (+, 0, −, 0); (f) the leakage currents across cell 1 for a single HV reversal sequence.

In Table IV, we show the combined analysis for the $\delta\nu$ channel (the last three rows of Table II) but without including the gradient coil feedback connection sign and, separately, with the **B** field sign included. As already mentioned, by not including the gradient coil sign we would be insensitive to an EDM but could detect the presence of electronic pickup or crosstalk in our data acquisition electronics. Similarly, by including the **B** field sign, we are insensitive to an EDM but could detect the presence of interference of the HV supply with the **B** field coil current supply. As seen in Table IV, there is no evidence for these systematic errors. We performed a similar analysis for the optical component reversals described above and again found no evidence for any anomalies. (Because different components were reversed for

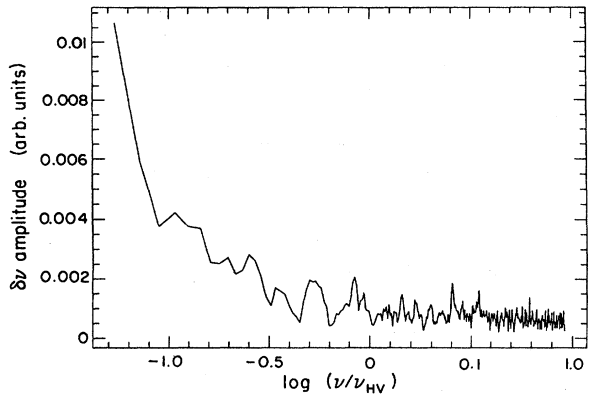

FIG. 5. Fourier transform of $\delta\nu$ for a typical run. $\nu_{\rm HV}=10^{-3}$ Hz.

different data sets, the results cannot be combined in the simple form of Table IV.)

Table V shows the steady-state values (average of the last two time segments) for some of the other data channels. The transmitted light channels are expressed as a normalized sum of, and difference between the two cells [i.e., $\mathscr{T}_{\rm sum}/\langle\mathscr{T}\rangle=(\mathscr{T}_1+\mathscr{T}_2)/\langle\mathscr{T}\rangle$ and $\mathscr{T}_{\rm diff}/\langle\mathscr{T}\rangle=(\mathscr{T}_1-\mathscr{T}_2)/\langle\mathscr{T}\rangle$]. By including the **B** field sign in the $\bar{\nu}$ channel, we are sensitive to a magnetic field from the HV supply that leaks through the magnetic shields, while without the **B** field sign, we would detect the effect of the HV switching on the **B** field coil current supply.

In Table V, the $(\mathscr{T}_{\rm sum}/\langle\mathscr{T}\rangle)(|E|)$ signal is expected from the Stark shift of the Hg vapor absorption line. Finally, the results for $B_{\rm amb}$ in Table V include data sets 4 and 5 only. For the earlier data sets, the fluxgate magnetometer was located at a different position further from the HV supply and showed no resolved signals. It is seen that the switching solenoids in the HV supply generate a small magnetic field at the magnetic shields. The correction we make for this field is described in Sec. VI.

The final step in the data analysis is to look for correlations between the $\delta\nu$ channel and all other data channels. The only significant correlations that were found were between the $\delta\nu(\mathbf{E})$ and $\delta\nu(|E|)$ channels of data sets 1 and 2, and the $\delta\nu(\mathbf{E})$ and $\mathscr{T}_{1,2}(\mathbf{E})$ channels of data sets 1 and 2. These correlations arise because the phase of the atomic oscillators in data sets 1 and 2 was set to make only $\bar{\nu}$ insensitive to changes in the light intensity. For the later data sets, where both $\bar{\nu}$ and $\delta\nu$ were made insensitive to changes in the light intensity, the correlations vanish. The contribution of the observed correlations to our systematic error estimate is described below.

V. POTENTIAL SYSTEMATIC EFFECTS

Here we discuss mechanisms by which application of the high voltage might generate a signal with the same signature as an EDM. A potential systematic effect would have to be correlated with the application of the high voltage, be asymmetric between the cells, and survive the experimental reversals described above. There is no evidence of any such contamination of the EDM results by systematic errors other than a small feed through the magnetic field from the HV solenoids, which will be discussed below.

A. Magnetic Effects

1. Leakage currents

A worrisome source of magnetic fields correlated with the high voltage is the steady-state leakage currents flowing between the electrodes of each cell. Approximately 100 s after the HV is applied, i_1 and i_2 reach their steady-state values of <1 pA (at 10 kV). These currents vary linearly with applied voltage, and hence are not likely to be corona discharges, but instead mainly Ohmic volume or surface currents at the quartz cell walls. Leakage currents can cause a frequency

TABLE II. Steady-state results for $\delta\nu$ by data set and high-voltage value. The final three rows list the results of the different data sets combined by HV value.

Data set	HV (kV)	No. runs	$\delta\nu$ (**E**) (nHz)	$\delta\nu$ (0) (nHz)	$\delta\nu$ ($\lvert E\rvert$) (nHz)
1	5	28	2.4±10.7	−26.7±11.1	−25.4±12.7
1	10	26	1.9±15.1	−6.5±10.7	−4.1±16.6
2	5	50	0.0±6.0	−4.3±5.6	9.5±7.4
2	10	50	11.4±7.4	15.6±6.1	−5.0±9.4
3	5	24	−3.8±5.0	2.7±6.6	3.5±9.2
3	10	24	−0.6±5.5	1.8±6.0	3.8±7.3
4	5	25	8.0±5.4	2.4±5.8	−6.2±7.0
4	10	24	−6.7±5.8	4.6±5.8	15.2±7.2
5	7	48	2.6±3.2	2.6±3.3	4.7±4.4
1–4	5	127	1.3±3.0	−2.4±3.3	−1.1±4.2
1–4	10	124	0.0±3.4	5.9±3.3	5.5±4.4

TABLE III. Results for the $\delta\nu$ channel for all time segments. The last column comes from the weighted average of the first three after dividing each result by the HV value, reflecting sensitivity to an EDM.

Signal	Time segment	5 kV (nHz)	7 kV (nHz)	10 kV (nHz)	Combined/kV (nHz/kV)
$\delta\nu$ (**E**)	1	7.9±3.6	−1.6±3.8	9.2±3.8	0.72±0.28
	2	3.7±3.9	0.4±3.9	12.4±3.9	0.83±0.30
	3	2.9±3.6	−1.8±3.8	7.3±3.8	0.44±0.28
	4	0.9±3.5	6.5±3.8	2.7±4.2	0.39±0.30
	5	2.5±4.1	−1.3±3.8	−2.5±4.3	−0.11±0.31
$\delta\nu$ (0)	1	−4.0±3.6	0.7±3.9	−5.9±3.8	−0.44±0.29
	2	4.2±3.5	1.4±3.9	5.7±3.6	0.52±0.28
	3	1.8±3.5	4.1±4.0	−0.1±3.6	0.19±0.28
	4	−1.7±3.8	2.9±3.9	3.4±3.6	0.26±0.28
	5	−0.6±4.2	2.2±3.8	6.2±4.5	0.41±0.32
$\delta\nu$ ($\|E\|$)	1	−1.3±4.4	0.0±5.5	2.2±5.0	0.08±0.38
	2	−3.2±4.8	4.3±5.2	3.6±5.4	0.26±0.40
	3	−4.6±4.9	7.4±5.8	−1.4±5.0	0.01±0.39
	4	2.5±4.6	4.2±5.1	−0.9±5.1	0.20±0.38
	5	−5.8±5.8	5.0±5.1	14.7±5.8	0.87±0.42

shift with the same signature as an EDM if the currents produce a magnetic field that projects onto **B**; however, these currents follow the lines of **E** from one electrode to the other, resulting in fields perpendicular to **B** to the extent that there is no helicity in the lines of **E**. Although such helicity should in fact be very small, suppose instead that the leakage currents were to flow in one complete loop in opposite directions around each cell; we calculate that the relative frequency shift between the two cells would still be less than 0.4 nHz, nearly an order of magnitude below our final statistical sensitivity.

Thus, leakage currents are not a limiting factor in the present experiment but they could limit future improvements in accuracy without an auxiliary measure of magnetic field in the cells.

2. Charging currents

As the HV increases from zero to its equilibrium value, transient charging currents of up to 0.1 nA/kV flow to the cell electrodes, and 0.3 nA/kV to the cell-holding vessel. These currents also should create magnetic fields mainly perpendicular to **B**, but these currents are so large they might well cause a measurable frequency shift. In fact, the data immediately after the HV ramp suggest such frequency shifts at the 10^{-27} e cm level in some data sets (see Table III), so we wait several spin-relaxation lifetimes before taking EDM data, well after the effects of the charging currents have fallen off.

A frequency shift would also occur if the charging currents left a residual magnetization in the magnetic shields. To test this, we added currents 100 000 times the normal size and looked for changes in the EDM signal. Based on this measurement we calculate that an effect of this type would be at least two orders of magnitude below our final sensitivity. Magnetization produced by charging currents would also appear with opposite sign on the 0^+ and 0^- dwells. A lack of signals on these channels gives us additional evidence that such effects were not present.

TABLE IV. Selected systematic error checks on the $\delta\nu$ channel.

Selected parameter	HV (kV)	$\delta\nu$(**E**) (nHz)	$\delta\nu$(0) (nHz)	$\delta\nu$($\|E\|$) (nHz)
Without gradient coil sign	5	−1.7±3.0	2.0±3.3	4.4±4.2
	7	−1.6±3.2	4.7±3.3	1.2±4.5
	10	−4.3±3.4	−0.6±3.3	2.0±4.3
With **B** field sign	5	−1.8±3.0	4.8±3.3	3.7±4.2
	7	2.1±3.2	6.5±3.3	−6.2±4.4
	10	−3.9±3.4	−3.9±3.2	−5.4±4.1

3. High-voltage solenoids

The polarity of **E** is set in the high-voltage supply by two 5-cm solenoids, which are separated by about 10 cm and located 3 m from the magnetic shields. The solenoids are active during the HV− and 0^- dwells and inactive during the HV+ and 0^+ dwells, and are situated so that when they are active their magnetic fields tend to cancel. The cancellation is incomplete, and a fluxgate magnetometer placed between the shields and the solenoids resolves the field from these solenoids at the 1.4-μG level in data sets 4 and 5. This field penetrates the shields and produces a small extra gradient signal, $\delta\nu_{\text{solenoid}}$, in the EDM data. To determine the size of $\delta\nu_{\text{solenoid}}$, we created a dipole source at the position of the solenoids that produced a field approximately 70 times the size of the solenoid field, and we measured the change in $\delta\nu$ for a given fluxgate signal, yielding the calibration 0.6 nHz/μG. We are uncertain of the exact calibration for earlier data sets, for which the magnetometer was located in a different position and showed no resolved signal, although the measured calibration agrees with the observed effect of occasional large ambient magnetic field disturbances in the lab

TABLE V. Steady-state signals of selected data channels. The results for B_{amb} include data sets 4 and 5 only.

Data channel	HV (kV)	**E**	0^+-0^-	$\lvert E\rvert$	Units
$\bar{\nu}$ with **B** sign	5	15±16	−6±16	−35±20	nHz
	7	5±18	−5±17	−12±21	nHz
	10	20±17	16±17	−14±20	nHz
$\bar{\nu}$ without **B** sign	5	25±16	14±16	43±20	nHz
	7	16±18	24±17	57±21	nHz
	10	34±17	14±17	65±20	nHz
$\mathscr{T}_{sum}/\langle\mathscr{T}\rangle$	5	47±76	−3±77	550±100	10^{-7}
	7	−1±81	−45±81	638±106	10^{-7}
	10	83±76	−29±80	1404±102	10^{-7}
$\mathscr{T}_{diff}/\langle\mathscr{T}\rangle$	5	−17±6	−3±7	14±9	10^{-7}
	7	16±9	−18±9	−2±12	10^{-7}
	10	41±7	46±7	−46±10	10^{-7}
i_1+i_2	5	26±1	−345±1	6±3	fA
	7	670±4	−365±4	11±8	fA
	10	284±1	−815±1	14±5	fA
i_1-i_2	5	−140±1	38±1	1±1	fA
	7	256±4	−286±4	4±6	fA
	10	−178±1	−156±1	−10±2	fA
B_{amb}	5	1.4±0.7	0.8±0.7	−0.3±0.7	μG
	7	1.4±0.5	0.7±0.5	0.4±0.5	μG
	10	1.4±0.6	1.5±0.6	−0.3±0.7	μG

that were recorded over the three years of data acquisition. The calibrated size of $\delta\nu_{solenoid}$ is smaller than the final statistical error bar on the EDM data. The same solenoid signal should appear also on the 0^+ and 0^- dwells, and thus the analysis of these dwells provide us with an independent check on the possible size of $\delta\nu_{solenoid}$ (and on other magnetic perturbations as well). Our treatment of the effect of $\delta\nu_{solenoid}$ on the EDM data is discussed in Sec. VI.

4. Cell movement

The cells sit in an inhomogeneous field of 5 μG/cm, due in part to the inhomogeneity of B_0. If the cells or the cell-holding vessel were to move as the HV is applied, we would expect a frequency shift in each cell. Any movement of the cells would appear as a disagreement between runs with **B** along $\hat{\mathbf{z}}$ and runs with B_0 along $-\hat{\mathbf{z}}$, contrary to our findings.

B. Light effects

Mechanisms by which changes in light intensity might create frequency shifts are particularly worrisome because we know that there is a change in light intensity correlated with the HV through the Stark shift. The center wavelength of the lamp is located to the side of the absorption line shape where a shift in line center will cause a maximum change in transmission. While such effects will predominantly be proportional to E^2, they can project onto an EDM signal to the extent that the HV reverses imperfectly or the changes are different between the two cells. This is of particular consequence in data sets 1 and 2, which showed correlations between $\delta\nu(\mathbf{E})$ and $\delta\nu(|E|)$. Furthermore, the most persistent correlation of the EDM data in data sets 1 and 2 is with the difference in dc light signals in the two cells ($\mathscr{T}_{diff}=\mathscr{T}_1-\mathscr{T}_2$). Note that this was before we properly zeroed the phase of each signal relative to the reference [see Sec. III, Eq. (19), and subsequent text].

1. Stark shift

We made an independent measure of the Stark shift in the EDM cells, taking data at 2.5, 5, 7, 10, 11, and 12 kV to verify the expected quadratic dependence on **E**. Measurement of the absorption lengths in each cell then allowed us to convert this fractional change in light intensity to a change in absorptivity. We find

$$\frac{\Delta\alpha}{\alpha}=(7.5\pm0.3\pm0.5)\times10^{-7}\ \ (\mathrm{kV/cm})^{-2}$$

and

$$\frac{\Delta\alpha}{\alpha}=(7.7\pm0.5\pm0.6)\times10^{-7}\ \ (\mathrm{kV/cm})^{-2}$$

for cell 1 and cell 2, respectively, where the first error comes from fitting our Stark data to a quadratic in **E** and the second error comes from determination of the absorption lengths in each cell.

2. Virtual light shift

The virtual light shift [15] (ac Stark effect) creates a shift in precession frequency of the atoms due to the electric field of the light, since $\langle\mathbf{E}^2\rangle\neq\mathbf{0}$. This shift has the form

$$\delta\nu=\delta\nu_{ls}\langle P_l\rangle\sin\theta+\pi\frac{\delta\nu_{ls}^2}{\omega_L}, \tag{22}$$

where $\langle P_l \rangle$ is the time-averaged circular polarization of the light and $90° - \theta$ is the angle between the light propagation direction and the precession field **B**. We measured $\delta\nu_{ls} = 4.5 \pm 0.5$ mHz in each cell at our normal light intensity. Taking our measured values of $\langle P_l \rangle = 0.5\%$ and $\theta < 1°$, we find for the two terms in Eq. (22)

$$|\delta\nu| < 0.4 \ \mu\text{Hz} + 1.2 \ \mu\text{Hz}.$$

This shift is constant to the extent that the light intensity remains constant, as do $\langle P_l \rangle$ and θ. The fractional change in light intensity with $|\mathbf{E}|$ is less than 10^{-4}, so we expect frequency shifts on $\delta\nu(|E|)$ to be of the order 0.1 nHz, further reduced by an order of magnitude for $\delta\nu(\mathbf{E})$ by the extent to which these shifts are the same in each cell.

3. Real light shift

A "real" light shift [15] could be caused by coherent precession of the atoms while in the excited state, where the gyromagnetic ratio of the excited state is approximately 1000 times that of the ground state. Collisions of mercury atoms with the buffer gas quench this coherence [21], so we do not consider this to be a possible mechanism.

4. Gradient in light intensity coupled to a magnetic field gradient

The precession frequency we measure comes from the average magnetic field in the cell, where the weighting of each portion of the cell comes from the light intensity there. When the HV is applied that weighting changes as the absorption changes (due to the Stark shift), so a static field gradient dB_z/dx gets translated to a frequency shift as measured by the cells. Such a shift would be quadratic in **E**, and only resemble an EDM to the extent that **E** reverses imperfectly and the field gradients or changes in light absorption differ between the two cells.

In order to estimate the size of such an effect, we did the calculation reproduced in Appendix III. From Eq. (C5), we find these frequency shifts to be given by

$$\delta\omega_{\text{grad}} = \Delta\omega_L \Gamma \frac{\Delta I}{I_0} \frac{a^2}{2\pi^2 D}, \tag{23}$$

where $\Delta\omega_L$ is the precession frequency change across the cell due to the field gradient, $\Gamma = \Gamma_p + \Gamma_r$ is the total polarization relaxation rate, ΔI is the change in light intensity (in this case the change correlated with the application of the electric field), a is the length of the cell, and D is the diffusion coefficient of the mercury atoms in the buffer gas.

To evaluate the size of this frequency shift we need to estimate D. We did this by looking at the effect on V^{in} as a known field gradient was applied and fitting it to the expected behavior from Eq. (C7):

$$V^{\text{in}} = V_0^{\text{in}} \left(1 - \frac{(\Delta\omega_L)^2 a^2}{2\Gamma D \pi^2} \right).$$

We obtained $a^2/D\pi^2 \approx 0.06$ s, a value consistent with estimates of the cell diffusion time based on the Hg—N_2 collision rate. Using this result in Eq. (23) along with the measured values of ΔI, Γ, and the usual field gradients (5 μG/cm), we would expect a signal on $\delta\nu(|E|)$ of 1 nHz, well below our statistical sensitivity. Furthermore, because this shift should show predominantly as an effect quadratic in E, the absence of any resolved $\delta\nu(|E|)$ signal in the final average leaves us confident that we are not limited by this effect.

5. Change in atomic polarization coupled to a magnetic field gradient

A change in polarization across a cell would similarly change the weighting of the magnetic fields from different spatial parts of the cell. We considered the effect of a field gradient along $\hat{\mathbf{z}}$ coupled to a change in polarization across the cell in $\hat{\mathbf{z}}$ arising from a changing interaction of the atoms with the HV electrodes when the HV is applied. (A similar effect would be if the spatial averaging of the cell changed due to a change in the thickness of the wax coating on the electrodes when the HV is applied.) This phase shift should also be predominantly an E^2 effect, but could have a greater projection onto our EDM signal since this mechanism would likely depend more critically on the wax coating of each individual cell electrode.

The analysis of such an effect can be carried out similarly to that of Appendix III and the effect of diffusion measured as in the previous section. Following the procedure of the previous section, measurements of V^{in} versus the applied gradient yielded an estimated frequency shift of 0.2 nHz in the normal running configuration with a field gradient of 5 μG/cm, far too small to be resolved.

C. Miscellaneous effects

1. Electronic pickup

Ground loops or high-frequency broadcasting from the HV supply can cause electronic pickup by other system signals. We have evidence for a persistent pickup of 50 μV correlated with $|E|$ on the digitized signals. This corresponds to a 1.3-nHz signal on $\delta\nu(|E|)$, which averages to zero because the signal does not change sign when the gradient correction current is reversed each day, while the sensitivity to an EDM does change sign. Cross talk between signals was measured to be insignificant and is demonstrated by the absence of correlations between system signals as discussed above.

2. Polar molecule in buffer gas

We explored several mechanisms by which the presence of the polar CO molecule in the cell buffer gas could cause frequency shifts when the HV was applied but found none that would produce measurable effects.

3. Magnetic dipole and electric quadrupole mixing of states of opposite parity

A change in absorption linear in **E** could come about from a mixing of states of opposite parity, giving small magnetic dipole and electric quadrupole components to allowed electric-dipole transitions. Such an effect was calculated for ^{199}Hg [22] and found to be negligible for our experimental geometry.

TABLE VI. Steady-state $\delta\nu$ channel corrected for the HV solenoid feed through. The second error in the Combined column is the systematic error associated with the HV solenoid correction.

Signal	5 kV (nHz)	7 kV (nHz)	10 kV (nHz)	Combined/kV (nHz/kV)
$\delta\nu$ (**E**)	1.1±3.0	1.7±3.2	−0.3±3.3	0.09±0.25±0.06
$\delta\nu(0)$	−2.6±3.3	2.1±3.3	5.6±3.3	0.33±0.25±0.05
$\delta\nu(\lvert E\rvert)$	−1.2±4.2	4.6±4.4	5.3±4.4	0.44±0.33±0.02

4. v×E *effects*

When the HV is applied, the atoms see a **v×E/c** magnetic field, which averages to zero to the extent that the motion of the atoms is isotropic. However, if the distribution of the pump light differs from that of the detection light, there will be a net magnetic field magnitude of the form

$$\delta B_z = A\,\frac{a}{\tau}\,\frac{E}{c}\sin\theta,$$

where A is a measure of the asymmetry between the pump and detection light intensities, a is the distance between the point where an atom gets pumped and where it gets detected, τ is the total pump time, and θ is the angle between **E** and **B**. We estimate the size of A to be $<1/18$, so taking a to be the cell diameter (2.5 cm), $\tau=20$ s, $\theta<5°$, and $E = 10$ kV/cm we conservatively estimate

$$\delta B_z = 0.7 \text{ pG},$$

which corresponds to a frequency shift of about 0.5 nHz. A second-order term quadratic in **E** will be orders of magnitude smaller than this.

VI. RESULTS

In this section we derive the final value and error for $d(^{199}\text{Hg})$. We make a small correction, $\delta\nu_{\text{solenoid}}$, to the central value of the raw result due to the magnetic field of the HV solenoids (see Sec. VA3), and calculate a systematic uncertainty for $d(^{199}\text{Hg})$ composed of two parts: an uncertainty derived from our measure of $\delta\nu(0)$, and the possible projection of $\delta\nu(|E|)$ onto $\delta\nu(\mathbf{E})$.

Of all the potential systematic errors studied, $\delta\nu_{\text{solenoid}}$ is the largest and also the only one that might have maintained the same sign and approximate size for much of the data. We correct the $\delta\nu$ channels for $\delta\nu_{\text{solenoid}}$ in data sets 4 and 5 by using the calibration from Sec. VA3, 0.6 nHz/μG, together with the average magnetometer signal from each of the two data sets. The resulting change, $\approx$0.8 nHz, is the only correction of any kind applied to the data, and is much smaller than the final statistical error. We make no correction in the earlier data sets because we cannot do so reliably, as discussed in Sec. VA3. The corrected $\delta\nu$ values are shown in Table VI.

To place a bound on the size of possible magnetic perturbations in our measurement of $\mathbf{d}(\mathbf{E}) \equiv \delta\nu(\mathbf{E})/V_{\text{HV}}$ we choose to use the results for $\mathbf{d}(0) \equiv \delta\nu(0)/V_{\text{HV}}$, since $\delta\nu_{\text{solenoid}}$ and other known magnetic perturbations that might change $\mathbf{d}(\mathbf{E})$ should also produce a comparable change in $\mathbf{d}(0)$. But $\mathbf{d}(0)$ is not sensitive to an EDM, and should be zero in the absence of systematic error. The final central value for $\mathbf{d}(0)$ in Table VI differs from zero by about 1.3σ (by 1.5σ if uncorrected for $\delta\nu_{\text{solenoid}}$). This offset is not resolved enough to indicate that a magnetic effect actually exists, and is much too large for known magnetic shifts, but it can be used to provide a conservative gauge of systematic uncertainty for $\mathbf{d}(\mathbf{E})$. Some magnetic effects, such as $\delta\nu_{\text{solenoid}}$, would appear with the same sign for $\delta\nu(\mathbf{E})$ and $\delta\nu(0)$, while effects such as magnetization of the magnetic shields from the charging currents would appear with the opposite sign. We have reanalyzed the data, separately adding and subtracting a correction for $\mathbf{d}(0)$, and obtained a systematic uncertainty in $\mathbf{d}(\mathbf{E})$ of ±0.33 nHz/kV. We believe the size of this uncertainty is safely conservative; it is four times the largest expected magnetic shift, $\delta\nu_{\text{solenoid}}$, discussed above.

A signal on the $\delta\nu(|E|)$ channel can feed through to the $\delta\nu(\mathbf{E})$ channel if the electric field reversal is imperfect. Although $\delta\nu(|E|)$ is consistent with zero, we have estimated nonetheless the possible projection of this signal onto $\delta\nu(\mathbf{E})$ by two methods: first by considering the asymmetry of the electric field reversal, and then using the results of the correlation analysis described above.

We can evaluate the asymmetry of the electric field reversal by comparing the change in light absorption due to the Stark shift for the two different polarities of the electric field. That is, we take the ratio of $\mathscr{I}_{\text{sum}}(\mathbf{E})$ to $\mathscr{I}_{\text{sum}}(|E|)$: for a perfect field reversal, $\mathscr{I}_{\text{sum}}(\mathbf{E})$ should vanish. (Note that this is more properly a measure of the asymmetry in $|E|$, which we would expect to be greater than that for **E** itself.) From Table V it is seen that this ratio is $(9\pm14)\%$, $(0\pm13)\%$, and $(6\pm5)\%$ for 5, 7, and 10 kV, respectively. Multiplying these ratios by $\delta\nu(|E|)$ for each value of the electric field strength and combining them as before, we find a potential systematic error contribution to $\mathbf{d}(\mathbf{E})$ of 0.03 nHz/kV.

We can also estimate the projection of a $|E|$ effect by looking for a possible correlation between $\delta\nu(\mathbf{E})$ and $\delta\nu(|E|)$ across the individual run results. Such a correlation existed for the 10-kV runs in data sets 1 and 2 due to background signals proportional to the dc light intensity that arose from imperfect settings of the phase of the reference signals to the PSD's, but was absent after data set 2. [Extrapolating $\delta\nu(\mathbf{E})$ to $\delta\nu(|E|)=0$ in data sets 1 and 2 leads to a change in final central value of <0.01 nHz/kV.] Nonetheless, to account for any possible correlation, for each data set and for each HV setting, we multiplied the slope given by the correlation analysis by the value of $\delta\nu(|E|)$ to obtain a possible correction to $\delta\nu(\mathbf{E})$, propagating the large uncertainty in the slope along with the statistical uncertainties. After recombining the results, we find that the correction to $\mathbf{d}(\mathbf{E})$ was at most 0.14 nHz/kV. Because this possible correction is larger than that given by the quadratic Stark shift analysis, we take 0.14 nHz/kV to be the systematic uncertainty of the feed through $\mathbf{d}(|\mathbf{E}|)$ onto $\mathbf{d}(\mathbf{E})$.

We find our final result from the weighted average of the last column in Table VI and add the three systematic error contributions in quadrature to obtain $d(^{199}\text{Hg}) = -(0.9 \pm 2.5 \pm 3.7)\times10^{-28}$ e cm, where the first error is statistical

TABLE VII. Upper limits (95% confidence level) on T-violating interactions set by the ^{199}Hg result reported here ($d<8.7\times10^{-28}e$ cm) compared with the best current limits from other experiments.

T-violating parameters	Ref.	Limit from ^{199}Hg	Best limit from other work	
		Hadronic		
Schiff moment (Q_S)	a	$Q_S<2.2\times10^{-11}$ e cm^3	$Q_S<1\times10^{-9}$ e fm^3	TlF [e]
$i\eta G_F(\bar{n}n)(\bar{n}\Gamma_5 n)/\sqrt{2}$	a	$\eta<1.6\times10^{-3}$	$\eta<2\times10^{-2}$	TlF [e]
$i\eta_q G_F(\bar{q}q)(\bar{q}\Gamma_5 q)/\sqrt{2}$	a	$\eta_q<3.4\times10^{-6}$	$\eta_q<4\times10^{-5}$	Neutron [f]
		Semileptonic		
$iC_T G_F(\bar{n}\Gamma_5\sigma_{\mu\nu}n)(\bar{e}\sigma^{\mu\nu}e)/\sqrt{2}$	a,d	$C_T<1.3\times10^{-8}$	$C_T<5\times10^{-7}$	TlF [e]
$iC_S G_F(\bar{n}n)(\bar{e}\Gamma_5 e)/\sqrt{2}$	a	$C_S<7\times10^{-7}$	$C_S<8\times10^{-7}$	Tl [g]
		Leptonic		
Electron (d_e)	a	$d_e<6\times10^{-26}$ e cm	$d_e<4\times10^{-27}$ e cm	Tl [g]
		Gauge model		
QCD phase ($\bar{\theta}_{\rm QCD}$)	a,b,c	$\bar{\theta}_{\rm QCD}<1.3\times10^{-9}$	$\bar{\theta}_{\rm QCD}<4\times10^{-10}$	Neutron [f]
Supersymmetry ($\epsilon^{\rm susy}$)	b,h	$\epsilon_q^{\rm susy}<7\times10^{-3}$	$\epsilon_q^{\rm susy}<1\times10^{-2}$	Neutron [f]
	b,h		$\epsilon_e^{\rm susy}<4\times10^{-2}$	Tl [g]
Multi-Higgs ($\epsilon^{\rm Higgs}$)	b	$\epsilon^{\rm Higgs}<0.7/\tan\beta$	$\epsilon^{\rm Higgs}<0.7/\tan\beta$	Tl [g]
Left-right sym. ($x^{\rm lr}$)	b	$x^{\rm lr}<2.0\times10^{-3}$	$x^{\rm lr}<1.3\times10^{-2}$	Neutron [f]

[a]See Refs. [26–30].
[b]See Ref. [13].
[c]We choose here the most recent calculation, Ref. [31].
[d]See Ref. [32].
[e]See Ref. [8].
[f]See Ref. [11] where $d_n<1\times10^{-25}$ e cm.
[g]See Ref. [10].
[h]See Ref. [33].

and the second is the systematic uncertainty. The other analysis described in Sec. IVB yields $d(^{199}\text{Hg})=-(1.2\pm2.2\pm3.5)\times10^{-28}$ e cm. For our final result, we average the central values and error bars from the two analyses to obtain

$$d(^{199}\text{Hg})=(-1.0\pm2.4\pm3.6)\times10^{-28}\ e\ \text{cm}. \quad (24)$$

After adding the statistical and systematic errors in quadrature, we can place an upper bound on the EDM of the ^{199}Hg atom by taking $|d|+1.78\sigma$:

$$|d(^{199}\text{Hg})|<8.7\times10^{-28}\ e\ \text{cm}\ (95\%\text{confidence}). \quad (25)$$

VII. THEORETICAL IMPLICATIONS

As mentioned at the beginning of the paper, there is now one generally accepted model at the fundamental gauge theory level that explains CP violation in K_0 decay and also is consistent with the failure to find an EDM at current experimental sensitivities. This model, now called the standard model, attributes CP violation to the extra phase angle that can occur at the quark-W boson vertex when there are three or more generations of quarks [13]. Granting this explanation of the K_0 results, there are still other potential sources of CP violation in gauge theories that would have a negligible effect on K_0 decay but would produce in a very natural way much larger EDM's than the standard model alone. In fact, a number of the most plausible and well motivated ideas in elementary particle physics that go beyond the standard model (such as low-energy supersymmetry, left-right symmetry, and models with 5 or more Higgs particles) actually lead to EDM's well within reach of current experiments. The failure to see an EDM in these experiments has serious implications for these ideas.

For example, supersymmetric theories can solve the gauge hierarchy problem (namely, the extreme smallness of the energy scale of electroweak unification, near 100 GeV, compared to the grand unification scale or gravity scale of $10^{16}-10^{19}$ GeV) only if supersymmetry is broken near the "low-energy" scale of 100 GeV. But low-energy supersymmetry automatically contains CP violation that has no natural reason to be very small, so EDM's would be expected to exist at currently measurable levels. We will show below that our present ^{199}Hg result, and other EDM limits as well, are beginning to place important constraints on supersymmetric theories.

Independently of specific gauge models, an atomic or molecular EDM would, in general, arise from an EDM distribution in the nucleus, from a T-violating force between electrons and nucleons, or from an intrinsic EDM of the electron itself, corresponding, respectively, to hadronic (quark-quark), semileptonic (electron-quark), or purely leptonic interactions as the chief source of the T violation. Table VII shows the limits on these various T-violating interactions set by our ^{199}Hg result, and for comparison includes limits set by other experiments as well. Table VII also shows the implications

of these T-violation limits for specific gauge models of CP violation.

^{199}Hg is sensitive to hadronic interactions through its nuclear Schiff moment Q_S, which measures the detectable, unshielded part of a nuclear EDM. A finite Schiff moment would reveal the presence of T-violating interactions between individual nucleons, and ultimately between quarks in the nucleus. The table shows the limit on the Schiff moment and the derived limit on η, the T-violating nucleon interaction coefficient. The limit on η in turn places important bounds on T-violating interactions at the quark level, such as a limit on the size η_q of the scalar-pseudoscalar quark-quark coupling shown in the table. ^{199}Hg is sensitive as well to the semileptonic tensor-pseudotensor coupling between electrons and nucleons, as shown by the limit on C_T in the table, and somewhat less sensitive to the semileptonic scalar-pseudoscalar coupling or to an intrinsic EDM of the electron.

Our ^{199}Hg result has implications for gauge models mainly through the bounds on quark couplings. It is clear from the table that gauge models of interest are becoming tightly constrained by the EDM limits. For example, it is expected that $\epsilon_q^{\rm susy}\approx 1$ if supersymmetry is broken near the electroweak energy scale [13], whereas $\epsilon_q^{\rm susy}<10^{-2}$ according to both the ^{199}Hg and the neutron EDM experiments, and $\epsilon_e^{\rm susy}<10^{-1}$ according to the atomic thallium EDM experiment. These values are small, and could begin to seem unnaturally small if future EDM experiments push back the limits still further. For multi-Higgs theories, $\epsilon^{\rm Higgs}\approx 1$ in most models containing more than one complex Higgs doublet, a value already being approached by the limits imposed by several experiments. In the case of left-right symmetric theories, the value of $x^{\rm lr}$ is already constrained to be below 4×10^{-3} by tests of the universality of the weak interactions [13].

ACKNOWLEDGMENTS

We thank E. Adelberger for providing a data analysis code, which we used as an independent check of the original data analysis, J. Cederberg, I. Khriplovich, and L. Sorensen for many helpful discussions, and R. Morley for fabrication of the lamps and cells used in the experiment. This work was supported by National Science Foundation Grant No. PHY-9206408.

APPENDIX A: SYSTEM NOISE

In this section, we estimate the ultimate shot-noise limit on the frequency measurement uncertainty and present evidence that, although the current experiment still has considerable room for improvement before approaching the ultimate limit, shot noise on the detected photons is the present limiting noise source in the system for modulation periods shorter than 1000 s.

The most illustrative way to estimate the shot-noise limit is through consideration of the minimum uncertainty in frequency $\delta\omega$ resulting from a measurement of N uncorrelated systems over an undisturbed time τ:

$$\delta\omega=\frac{1}{\tau\sqrt{N}}. \tag{A1}$$

Our experiment is based on measurement of the change in spin precession frequency of an ensemble of atoms for parallel and antiparallel applied electric and magnetic fields. Since there are N atoms, corresponding to N uncorrelated quantum systems, the uncertainty in the frequency difference, assuming a measurement interval for each of the atoms τ is

$$\delta\omega=\sqrt{2}\frac{1}{\tau\sqrt{N}}, \tag{A2}$$

where the factor $\sqrt{2}$ reflects the extra uncertainty in the difference between the two measurements. After many such measurements, over a time $T\gg\tau$ (total number of differential measurements is $T/2\tau$), the final uncertainty is

$$\delta\omega=\sqrt{2}\frac{1}{\tau\sqrt{N}}\sqrt{\frac{2\tau}{T}}=\frac{2}{\sqrt{\tau TN}}. \tag{A3}$$

Here τ is the atomic coherence time,

$$\tau^{-1}=\Gamma_p+\Gamma_r, \tag{A4}$$

where Γ_p is the pump rate and Γ_r is the wall relaxation rate.

The net EDM sensitivity, for the differential frequency measurement of a single cell, is determined through use of

$$\omega=4dE/\hbar, \tag{A5}$$

where, as before, d is the EDM and E is the applied electric field. In normal operation of the experiment, two cells are used with oppositely directed electric fields; this leads to a net factor of $\sqrt{2}$ improvement in sensitivity. Thus, the ideal corresponds to a dipole uncertainty

$$\delta d=\frac{\hbar}{2E}\frac{1}{\sqrt{2\tau TN}}. \tag{A6}$$

Under typical operating conditions, $\tau\approx 20$ s and $E=10$ kV/cm; N is estimated from absorption measurements to be about 4×10^{13} in the 4.9-cc cell. In one day of measuring, the ideal uncertainty would be

$$\delta d=3\times10^{-30}\ e\ \text{cm}. \tag{A7}$$

There are a number of factors that reduce this sensitivity in the current version of the experiment. First, the atomic oscillator modulation amplitude corresponds to only a fraction of the photon flux, 1/8, under normal operation of the atomic oscillator. Note that this represents a direct reduction in the signal-to-noise ratio, unlike the other reduction factors described below, which enter only as the square root.

The following reduction factors enter as the square root. The light collection efficiency is about 25%, the photomultiplier efficiency is 10%, the fraction of incident photons, which are ultimately detected, i.e., the net transmitted photon flux, is about $e^{-1.5}=0.22$, and the fraction of data over the time T, which contains useful EDM information, is 1/8 (system response wait periods and data taken at zero high voltage do not contribute to the EDM measurement). These and

some smaller factors total $\sqrt{3800}$. Thus, the overall sensitivity reduction factor is 500, which gives a daily EDM sensitivity of

$$\approx 1.3\times 10^{-27}\ e\ \text{cm}, \tag{A8}$$

which is rather close to the uncertainty of the best data sets. On average, the experiment sensitivity in one night is 2.7×10^{-27} e cm, but the best runs give an uncertainty less than 2.0×10^{-27} e cm.

Figure 5 is a Fourier transform of a data run. The difference signal has a $1/f$ spectrum with a corner at a frequency corresponding to a period of 1500 s. The electric field reversal period is 1000 s. In Fig. 5, the noise is "white" for sufficiently high frequencies, but the electric field reversal frequency is low enough so that there is noise in addition to the shot-noise estimate described above. The source of the $1/f$ noise is unknown, but appears to be associated with noise in the field gradient and drifts in the light polarization phase angle. The latter are due to thermal stresses changing the properties of the quarter-wave plate, and to mechanical noise in the modulator mechanism.

We have performed a number of studies that demonstrate that the limiting white noise is in fact shot noise in the detected photons. First, we measured the photomultiplier current and inferred the detected photon count from the manufacturer's quoted photomultiplier gain. The computed shot noise agrees with the actual measured noise, but it is difficult to estimate the uncertainty in this method.

As a next step, we investigated the dependence of various noise sources on the pump rate in order to compare with measured short-term atomic oscillator differential frequency as a function of light intensity. Two sources of light-induced frequency noise are intensity fluctuations and photon shot noise. To estimate the dependence of these noise sources on pump rate, consider the intrinsic sensitivity of the atomic oscillator, which can be inferred from Eqs. (15) and (16):

$$\delta\omega = \frac{(\Gamma_p+\Gamma_r)^2}{\Gamma_p}\,\sigma^{-1}, \tag{A9}$$

where σ describes the (fractional) noise on the light. This relationship can be understood as follows: The linewidth is given by $\Gamma_p+\Gamma_r$ while the net atomic polarization is determined by $\Gamma_p/(\Gamma_p+\Gamma_r)$, with $\Gamma_p \propto \Phi$, the net photon flux. In the case where shot noise dominates, $\sigma \propto \sqrt{\Phi}$, which leads to

$$\delta\omega = \frac{(\Gamma_p+\Gamma_r)^2}{\Gamma_p^{3/2}} \propto \frac{(a+b\Phi)^2}{\Phi^{3/2}}\,. \tag{A10}$$

Non-shot-noise intensity fluctuations give a fractional noise σ independent of the light intensity, leading to a frequency noise dependence on pump intensity simply proportional to Eq. (A9), or

$$\delta\omega \propto \frac{(a+b\Phi)^2}{\Phi}\,. \tag{A11}$$

Phase noise associated with, for example, the mechanical modulator, gives a frequency noise proportional to the pump intensity. This is because the linewidth increases with increased pumping, and the frequency noise generated by a phase noise is simply proportional to the linewidth. Finally, real magnetic field noise is independent of the pump rate.

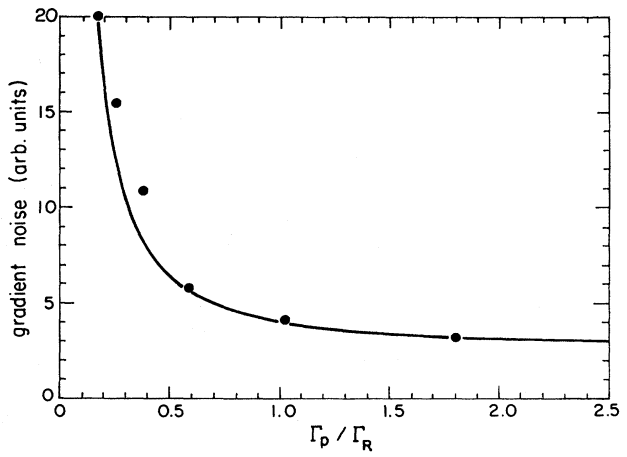

FIG. 6. Noise on the gradient channel as a function of pump rate. Dots show data points, solid line shows best fit to Eq. (A10).

The noise as a function of pump intensity (Φ) was measured by reducing the incident light with a neutral density filter and measuring the rms fluctuations in the difference signal between 20-s averaging periods. The results are shown in Fig. 6. The functional form given by shot noise, Eq. (A10), gives the best description of the observed noise; a best fit to Eq. (A10) is also shown in Fig. 6, where the constants, a and b, were adjusted. The broad minimum predicted by Eq. (A10) is unmistakable, and the inferred parameters $b\Phi/a = 1.85 = \Gamma_p/\Gamma_r$ at the highest light intensity agrees with direct measurements of $\Gamma^{-1}=20$ s and $\Gamma_r^{-1}=60$ s, which imply $\Gamma_p/\Gamma_r=2$.

As a further test, a 24-h run was taken with a neutral density filter between the cells and photomultiplier tubes, which reduced the detected photon intensity by a factor of 10. The increased uncertainty run agreed with the expectation computed from shot noise. Based on the consistency among the various methods of determining the noise, we are confident that at the present level of sensitivity, the dominant system noise for modulation periods out to 1000 s is shot noise on the detected photons.

APPENDIX B: Hg VAPOR CELLS

We describe here the technique used to make the cells used in the EDM experiment. This technique is the result of four years of extensive development with the goal of producing cells with stable Hg density, long spin-relaxation times, electrodes for application of the HV, and leakage currents of $\sim$ 0.1 pA/kV.

The main cylinder, endplates, and fill stem of the cells are made of high-purity, synthetically produced fused silica (Heraeus Amersil Suprasil I). The fill stem and body tubing (see Sec. IIIE) are joined to form a cell "blank." The tubing is washed thoroughly in hot chromic acid cleaning solution (a saturated solution of CrO_3 in hot concentrated H_2SO_4) using the procedure described in [23]. After the stems are attached to the cell bodies, the blanks are washed again, annealed at 1100 °C for 1–2 h, cooled slowly, then washed a

third time. We believe that this washing procedure has contributed significantly to the reduction of cell leakage currents. The bodies of the blanks are dipped in a 10% solution of a siliconizing agent in acetone, which provides a nonwettable surface coating on the cell walls and increases the spin lifetime at room temperature.

The inner surface of the cell endplates are coated with tin-oxide (SnO_2) to provide a conductive surface for the application of electric fields. We use the recipe given by Coghill [24], which gives a homogeneous surface coating having a resistance of between 1–10 MΩ across the plate. It is necessary to have the electrode on the inner side of the endplate in order to have an undiminished electric field inside of the cells. The endplates and blanks are glued together with Varian Torr-Seal high-vacuum epoxy taking care that as little excess as possible remains on the inside of the cell. The inner surfaces of the cells must be free of dust and must not be touched. We used freon dust chaser to lightly spray disks and blanks before assembly.

After the epoxy has dried, the cells are attached to the vacuum system with the fill stems horizontal and the surface of the endcaps vertical; this orientation greatly simplifies the process of putting the wax in the cells and monitoring the absorption of light as Hg is let into the cells. Also attached to the vacuum system are a side arm with a small amount of wax (dotriacontane), an ampoule with isotopically enriched (95%) metallic ^{199}Hg, a 3-l bottle containing an oxygen-free mixture of 95% N_2 and 5% CO at about 700 torr, and an absolute pressure gauge for measuring the buffer gas pressure in the cells.

If oxygen is present in the cell, we found that in the presence of UV light the mercury in the cell can oxidize, gradually depleting the Hg density. To avoid this, trace amounts of oxygen were removed from the buffer gas by bubbling it through a mercury-magnesium amalgam. The oxidation of mercury probably begins with the formation of ozone through a photoensitized reaction with an excited state mercury atom as the catalyst. Ozone reacts with ground state mercury atoms to produce HgO. For low concentrations of oxygen and mercury, the formation of ozone and the subsequent disappearance of the mercury is almost certainly enhanced by the presence of nitrogen, which is known to quench mercury to its metastable state [21]. This allows the excited state mercury atom more time to "find" an oxygen molecule.

In early versions of these cells, the spin-relaxation lifetimes slowly degraded over time. Although the exact process for this degradation in not understood, there is strong evidence that the mercury atoms are relaxed by atomic hydrogen, which is liberated from the wax through photosensitized reactions with excited state mercury atoms or direct reactions with the UV light. The CO serves to stabilize the spin-relaxation lifetime of the cells by acting as a getter for any hydrogen that is liberated. CO will react with hydrogen in the presence of excited state mercury atoms to form formaldehyde ([25], p. 82). The stabilized spin-relaxation lifetime is lower than the lifetimes without CO added to the cells for reasons that are not understood. Cells made with lower concentrations of carbon monoxide had the same limiting lifetime.

The system is pumped to 5×10^{-7} torr, then the wax is heated slightly and the seal off point for each cell is heated to just below the softening point (white hot) to remove any impurities. The cells are then baked at 120 °C for 8–10 h. A small amount of wax is then gently chased into each cell with a hand torch, using just enough heat to move the (liquid) wax but not so much that it vaporizes. The amount of wax put into each cell is critical. It must be enough to completely cover both endplates, but then the coating must be reduced to a thin layer with the extra wax chased off the cell body and into the fill stem after the cells are removed from the vacuum system. The cells are then cycled several times in the presence of ^{199}Hg vapor between room temperature and the melting point for the wax (≈70 °C). After the cycling, the seal-off points are again heated to chase all wax off of these points.

To determine the amount of Hg vapor in the cells we monitor the transmission of resonance radiation through the cells during the filling process. We use an ^{204}Hg lamp similar to the one described in Sec. IIIA, along with an aluminum coated mirror and solar blind photomultiplier situated so that the mirror reflects the light up through the cell and into the photomultiplier. First the cell is filled with the room temperature vapor pressure of ^{199}Hg, which scatters all resonant light, and filled with 300 torr of buffer gas, allowing us to determine the portion of nonresonant light in the lamp (normally about 20%). The cells are then pumped out and filled with a smaller amount of ^{199}Hg and about 300 torr of N_2/CO mixture to achieve a final absorption of between 1.2 and 1.8 absorption lengths. After the cells are filled, they are sealed off from the vacuum system using a hand held torch, leaving a stem of about 1 − 1.5 in.

After the cells are sealed, the wax must be remelted to redistribute it inside the cells. The wax must form a very thin layer over the SnO_2 endplates, all wax must be driven off the cylindrical cell body, and all extra wax must be chased into the fill stem. The only test of whether the wax has been melted properly is by testing the lifetime (this indicates how well the electrodes are covered), and the leakage current (this indicates how well the wax has been chased off the cell walls). Out of a batch of six cells normally one or two were successfully melted. The cells may have to be remelted as many as 50–100 times before the cell has a long spin-relaxation lifetime, and the above conditions have been met.

APPENDIX C: CALCULATION OF THE EFFECT OF A MAGNETIC FIELD GRADIENT

In Sec. V, we considered a mechanism by which a static magnetic field gradient can give rise to frequency shifts when a light intensity gradient is also present. Here we treat the general problem of a magnetic field gradient and derive the expressions needed to estimate the size of the specific effect discussed in Sec. V.

We analyze the atomic polarization by the method developed in Sec. II, and take account of the spatial variation of the atomic polarization by including a diffusion term $D\nabla^2\mathbf{P}_A$ in Eq. (7) of that section. Thus, we begin with the equation

$$\left(\frac{d\mathbf{P}_A}{dt}\right) = -\gamma\mathbf{P}_A\times\mathbf{B}-\Gamma\mathbf{P}_A+\Gamma_p\mathbf{P}_l+D\nabla^2\mathbf{P}_A\,, \qquad \text{(C1)}$$

where $\mathbf{B}$ is now a function of position, and as usual $\Gamma=\Gamma_p+\Gamma_r$. We orient the z axis along $\langle\mathbf{B}\rangle$ and simplify to spatial variation of B_z only along $\hat{\mathbf{x}}$, the light propagation direction. As in Sec. II, we transform to a coordinate system rotating about z, and obtain the analog of Eq. (12):

$$\left(\frac{d\mathbf{P}_A}{dt}\right)_{\text{rot}}=[-(\omega_L-2\omega_m)\mathbf{P}_A\times\hat{\mathbf{z}}-\Gamma\mathbf{P}_A+\tfrac{1}{2}\Gamma_p\hat{\mathbf{y}}+D\mathbf{P}_A'']_{\text{rot}}, \tag{C2}$$

where the primes denote spatial derivatives along $\hat{\mathbf{x}}$ in the *laboratory* (nonrotating) frame. We have dropped terms in B_x and B_y, which appear because of field inhomogeneities but have a negligible effect in the large ω_L limit appropriate for our experimental conditions.

For simplicity we assume constant Γ_r over the cell volume and no spin relaxation at the cell walls, which if the walls are located at $x=\pm a/2$ leads to the boundary condition $\mathbf{P}_A'(a/2)=\mathbf{P}_A'(-a/2)=0$. [One would set $\mathbf{P}_A'(\pm a/2)=\mp(a/2D)\langle\mathbf{P}_A\rangle(\Gamma_r)_{\text{wall}}$ to include the effect of any wall relaxation.] It is convenient to express the magnetic field gradient by expanding the Larmor frequency in a Fourier series; here we will keep only the leading nonzero term

$$\omega_L=\omega_L^0+\Delta\omega_L\sin\left(\frac{\pi x}{a}\right),$$

where $\Delta\omega_L$ is thus a measure of the change in magnetic field over the cell. This change is very small (<1 μG) in our experiment, and the diffusion is rapid, i.e., under our conditions $(D/a^2)\gg\Gamma\gg\Delta\omega_L$. Thus, we adopt a perturbation approach to solving Eq. (C2) subject to the given boundary conditions, and expand the steady-state solution in powers of $\Delta\omega_L$, while retaining only terms through first order in $1/D$. Using the notation of Eq. (13) (to which our result reduces in zeroth order), we obtain near resonance ($|\omega_L^0-2\omega_m|\ll\Gamma$):

$$(\mathbf{P}_A)_{\text{rot}}\approx\frac{\Gamma_p}{2\Gamma^2}\begin{pmatrix}-(\omega_L^0-2\omega_m)-\dfrac{\Delta\omega_L\Gamma a^2}{D\pi^2}\sin\left(\dfrac{\pi x}{a}\right)\\ \Gamma-\dfrac{(\Delta\omega_L)^2a^2}{2D\pi^2}\\ 0\end{pmatrix}, \tag{C3}$$

where we have kept only the leading-order term in $\Delta\omega_L$ for each component.

We weight each point of the cell by the light intensity there in order to find the average detected change in frequency, $\delta\omega_{\text{grad}}$, and in decay rate, $\delta\Gamma_{\text{grad}}$, produced by the field gradient. Expanding I in a Fourier series, and as with ω_L keeping only the leading nonzero term

$$I=I_0+\Delta I\sin\left(\frac{\pi x}{a}\right),$$

we find near resonance

$$\frac{1}{I_0 a}\int_{-\frac{a}{2}}^{\frac{a}{2}}(\mathbf{P}_A)_{\text{rot}}I\,dx=\frac{\Gamma_p}{2\Gamma^2}\begin{pmatrix}-(\omega_L^0-2\omega_m)-\delta\omega_{\text{grad}}\\ \Gamma-\delta\Gamma_{\text{grad}}\\ 0\end{pmatrix}, \tag{C4}$$

where

$$\delta\omega_{\text{grad}}=\Delta\omega_L\Gamma\frac{\Delta I}{I_0}\frac{a^2}{2\pi^2D} \tag{C5}$$

and

$$\delta\Gamma_{\text{grad}}=\Delta\omega_L^2\frac{a^2}{2D\pi^2}. \tag{C6}$$

Equation (C6) may be used to determine the diffusion coefficient D by applying a large known magnetic field gradient and measuring the change in relaxation rate. To see the effect on V^{in} of the change from Γ_r to $\Gamma_r+\delta\Gamma_{\text{grad}}$, we recognize that for small $\delta\Gamma_{\text{grad}}$

$$V^{\text{in}}\propto\frac{\Gamma_p}{\Gamma}\approx\frac{\Gamma_p}{\Gamma_p+\Gamma_r}\left(1-\frac{\delta\Gamma_{\text{grad}}}{\Gamma_p+\Gamma_r}\right).$$

Substituting in Eq. (C6) for $\delta\Gamma_{\text{grad}}$ we find

$$V^{\text{in}}=V_0^{\text{in}}\left(1-(\Delta\omega_L)^2\frac{a^2}{2\Gamma D\pi^2}\right). \tag{C7}$$

We can thus determine the diffusion coefficient needed in Eq. (C5) by looking at V^{in} as a function of a known applied field gradient.

As discussed in Sec. V, to estimate the size of the frequency shift in Eq. (C5), we still need to know $\Delta\omega_L$ under the conditions of the experiment, as well as the total pump rate Γ and the fractional change in light intensity when the high voltage is applied (Stark shift). It is interesting that geometric factors, expressed here by the size a of the cell, drop out when we use the value of D found by Eq. (C7).

[1] J. H. Christenson, J. W. Cronin, V. L. Fitch, and R. Turlay, Phys. Rev. Lett. **13**, 138 (1964).

[2] N. F. Ramsey, Phys. Rep. **43**, 410 (1978).

[3] P. G. H. Sandars and E. Lipworth, Phys. Rev. Lett. **13**, 718 (1964).

[4] P. G. H. Sandars, Phys. Lett. **14**, 194 (1965); Phys. Rev. Lett. **19**, 1396 (1967).

[5] See E. S. Ensberg, Bull. Am. Phys. Soc. **7**, 534 (1962) for the early work of H. G. Dehmelt and E. S. Ensberg.

[6] T. G. Vold, F. Raab, B. Heckel, and E. N. Fortson, Phys. Rev. Lett. **52**, 2229 (1984).

[7] J. P. Jacobs, W. M. Klipstein, S. K. Lamoreaux, B. R. Heckel, and E. N. Fortson, Phys. Rev. Lett. **71**, 3782 (1993).

[8] D. Cho, K. Sangster, and E. A. Hinds, Phys. Rev. Lett. **63**, 2559 (1989).

[9] S. A. Murthy, D. Krause, Jr., Z. L. Li, and L. R. Hunter, Phys. Rev. Lett. **63**, 965 (1989).

[10] K. Abdullah, C. Carlberg, E. D. Commins, Harvey Gould, and

Stephen B. Ross, Phys. Rev. Lett. **65**, 2347 (1990); most recent results are in E.D. Commins, S.B. Ross, D. DeMille, and B. C. Regan, Phys. Rev. A **50**, 2960 (1994).
[11] K. F. Smith *et al.*, Phys. Lett. B **234**, 191 (1990).
[12] I. S. Altarev *et al.*, Phys. Lett. B **267**, 242 (1992).
[13] S. M. Barr, Int. J. Mod. Phys. A **8**, 209 (1993).
[14] S. K. Lamoreaux, J. P. Jacobs, B. R. Heckel, F. J. Raab, and E. N. Fortson, Phys. Rev. Lett. **59**, 2275 (1987).
[15] W. Happer, Rev. Mod. Phy. **44**, 169 (1972).
[16] W. E. Bell and A. L. Bloom, Phys. Rev. Lett. **6**, 280 (1961).
[17] See, for example, A. Yariv, *Optical Electronics*, 4th ed. (HRW Saunders, Philadelphia, 1991).
[18] J. P. Jacobs, Ph.D. thesis, University of Washington, 1991.
[19] S. K. Lamoreaux, J. P. Jacobs, B. R. Heckel, F. J. Raab, and E. N. Fortson, Phys. Rev. A. **39**, 1082 (1989).
[20] See, for example, K. G. Beauchamp, *Walsh Functions and Their Applications* (Academic Press, New York, 1975); or H. F. Harmuth, *Transmission of Information by Orthogonal Functions* (Springer-Verlag, Berlin, 1969).
[21] G. Herzberg, *Atomic Spectra and Atomic Structure* (Dover Publications, New York, 1944).
[22] S. K. Lamoreaux and E. N. Fortson Phys. Rev. A **46**, 7053, (1992).
[23] F. Rosebury, *Handbook of Electron Tube and Vacuum Techniques* (Addison-Wesley, Reading, MA, 1972).
[24] H. D. Coghill, *Proceedings of the Eleventh Symposium on the Art of Glassblowing*, edited by G. Sites (The American Scientific Glassblowers' Society, Wilmington, DE, 1966).
[25] A. C. G. Mitchell and M. W. Zemansky, *Resonance Radiation and Excited Atoms* (Cambridge University Press, Cambridge, England, 1934).
[26] I. B. Khriplovich, in *Proceedings of the Eleventh International Conference on Atomic Physics*, edited by S. Haroche, J. C. Gay, and G. Grynberg (World Scientific, Singapore, 1989).
[27] V. V. Flaumbaum, I. B. Khriplovich, and O. P. Sushkov, Phys. Lett. **162B**, 213 (1985).
[28] V. V. Flaumbaum, I. B. Khriplovich, and O. P. Sushkov, Nucl. Phys. **A449**, 750 (1986).
[29] V. M. Khatsymovsky, I. B. Khriplovich, and A. S. Yelkhovsky, Ann. Phys. (N.Y.) **186**, 1 (1988); V. M. Khatsymovsky and I. B. Khriplovich, Phys. Lett. B **296**, 219 (1992).
[30] W. C. Haxton and E. M. Henley, Phys. Rev. Lett. **51**, 1937 (1983).
[31] Kar Lee, Ph.D. thesis, University of Washington, 1994.
[32] A.-M. Mårtensson-Pendrill, Phys. Rev. Lett. **54**, 1153 (1985).
[33] W. Fischler, S. Paban, and S. Thomas, Phys. Lett. B **289**, 373 (1992).